

Peer review status:

This is a non-peer-reviewed preprint submitted to EarthArXiv.


Lorenz Energy Cycle Climatology for the Southwestern Atlantic Cyclones


Danilo Couto de Souza^{1,2*}, Pedro Leite da Silva Dias¹,
Carolina Barnez Gramscianinov³, Ricardo Camargo¹

¹Institute of Astronomy, Geophysics and Atmospheric Sciences, São
Paulo University, Rua do Matão, 266, São Paulo, 05508-090, São Paulo,
Brazil.

²Climate Risk Initiative, IRB(re), Av. República do Chile, 330 - 4o
andar, Rio de Janeiro, 20031-170, Rio de Janeiro, Brazil.

³Institute for Coastal Systems Analysis and Modeling,
Helmholtz-Zentrum Hereon, Max-Planck-Straße, 1, Geesthacht, 21502,
Schleswig-Holstein, Germany.

*Corresponding author(s). E-mail(s): danilo.oceano@gmail.com .

Contributing authors: pldsdias@gmail.com .

cbgramscianinov@gmail.com ; ricamarg@usp.br .

Abstract

This study presents a climatological assessment of the Lorenz Energy Cycle (LEC) applied to South Atlantic cyclones, using a Semi-Lagrangian framework. Over 6,700 cyclones were identified from ERA5 reanalysis (1979–2020), and LEC components were computed and averaged across four objectively defined life cycle phases: incipient, intensification, mature, and decay. Results reveal a coherent energy transfer structure: baroclinic conversions dominate during intensification, while barotropic conversions peak during the mature phase and reach magnitudes 2–3 times larger than baroclinic counterparts. Diabatic generation of eddy available potential energy plays a secondary but relevant role, particularly during intensification, occasionally surpassing baroclinic contributions. Eddy kinetic energy imports are most significant during the early phases, reinforcing development. Despite substantial variability among systems, an EOF analysis shows that most cyclones share a common energy structure, with variability manifesting as amplification or suppression of specific pathways. The leading EOFs are linked to differences in cyclone intensity, genesis region, and seasonality. Among the most intense systems, distinct clusters emerge with varying energetic

configurations, some dominated by baroclinic processes, others by barotropic conversions or enhanced diabatic generation. These findings demonstrate that South Atlantic cyclones encompass a spectrum of dynamical behaviors and can be classified based on their energy cycle characteristics. This study provides the first large-sample application of the Semi-Lagrangian LEC to extratropical cyclones in the South Atlantic and highlights the importance of barotropic processes in their development. The results offer a robust framework for interpreting cyclone energetics and establish a comprehensive baseline for classifying these systems.

Keywords: Cyclone energetics, Baroclinic conversion, Barotropic conversion, Latent heat release, South Atlantic cyclones

Acknowledgements

The first author would like to thank the Laboratory of Applied Meteorology for Regional Meteorological Systems (MASTER) for providing the data processing infrastructure. Special thanks are extended to Jean Peres and Djalma Vieira for their invaluable technical assistance and support in the laboratory, which contributed significantly to the success of this research. CBG acknowledges the Helmholtz European Partnership “Research Capacity Building for Healthy, Productive and Resilient Seas” (SEA-ReCap, grant no. PIE-0025).

1 Introduction

Cyclones play a crucial role in the Earth’s climate system by redistributing heat, moisture, and momentum across different regions. These dynamic weather systems, contribute to the global energy balance by transferring energy from the tropics to higher latitudes. Understanding cyclone behavior is essential for improving climate projections and assessing future climate change impacts. In South America, surface cyclones influence precipitation regimes across the continent (Reboita et al., 2010, 2018; de Souza et al., 2022) often contributing to extreme rainfall events (e.g., de Souza and da Silva, 2021; de Souza et al., 2024), and are associated with severe meteorological hazards such as intense winds (Cardoso et al., 2022; de Souza and da Silva, 2021), high sea waves (da Silva et al., 2025; Gramscianinov et al., 2023), and storm surges along coastal areas (Leal et al., 2023; Tecchio et al., 2024). These extreme events can have profound socioeconomic impacts, including damage to coastal infrastructure, disruptions to port operations, and interruptions in oil and gas exploration. This is particularly critical in the southeastern region of South America, where large metropolitan areas, such São Paulo, Rio de Janeiro and Buenos Aires are located, as well as the Port of Santos, the largest in Latin America.

The Lorenz Energy Cycle (LEC) is a valuable framework for understanding the conversion and flow of energy within the atmosphere, particularly in relation to synoptic and large-scale processes (Lorenz, 1967). It divides the atmospheric energy budget into four main reservoirs: kinetic and available potential energy, both for zonal (mean

flow) and eddy components. Lorenz (1955) formulated the concept of available potential energy (APE), building upon Margules (1903) concept of energy based on the hypothetical adiabatic redistribution of atmospheric mass. The LEC serves as a foundational tool for quantifying and understanding atmospheric dynamics, by tracking energy transformations and explaining how these forms of energy are generated by adiabatic processes and dissipated by friction.

Substantial efforts have been made to estimate the LEC components for the global circulation (e.g., Muench, 1965; Wiin-Nielsen, 1968; Hu et al., 2004; Li et al., 2007; Oort, 2018), to assess its projected changes under climate change scenarios (e.g., Hernández-Deckers and von Storch, 2010; Veiga and Ambrizzi, 2013; Pan et al., 2017; Michaelides, 2021), and to explore its relationship with phases of the El Niño–Southern Oscillation (Gutierrez et al., 2009). The LEC framework has also been applied in a range of contexts, from idealized baroclinic wave simulations (Kirshbaum et al., 2018; Rantanen et al., 2019), to rotating annulus experiments (Young, 2014), and even to the atmospheres of other planets (e.g., Read et al., 2020). In contrast, studies examining the LEC in relation to cyclonic systems are more limited and primarily consist of case studies. These have typically focused on tropical (Brennan and Vincent, 1980; Veiga et al., 2008), subtropical (Michaelides, 1987; Dias Pinto et al., 2013; Pezza et al., 2014; Cavicchia et al., 2018), and extratropical cyclones (Michaelides, 1992; Wahab et al., 2002; Bulic, 2006; Pezza et al., 2010; Dias Pinto and Rocha, 2011). Noteworthy contributions include the work of Black and Pezza (2013), which investigated explosive cyclones across all major ocean basins over a 32-year period and identified a universal signature of explosive cyclogenesis, and Okajima et al. (2021), which quantified the contribution of migratory cyclones to global energetics, highlighting their role in accelerating westerly winds worldwide.

Although the original formulation by Lorenz (1967) was intended for global-scale studies, analyzing specific atmospheric regions is valuable for understanding the mechanisms driving the development of individual systems, such as cyclones, and the energy conversions throughout their life cycle. The initial framework for such regional analysis was introduced by Muench (1965), who studied Northern Hemisphere stratospheric circulation during winter. Subsequent formulations by Dutton and Johnson (1967), Vincent and Chang (1973), and Smith (1980) refined the approach, but it was only with Brennan and Vincent (1980) that a generalized set of equations, including both eddy and zonal components of kinetic and APE for limited regions in the troposphere, was established. However, cyclones are mobile systems that often traverse large regions (Hoskins and Hodges, 2002; de Souza et al., 2024, e.g.). Since these studies employ the LEC within an Eulerian framework, the computational domains required to analyze cyclone energetics can become quite large (Black and Pezza, 2013, e.g.), potentially incorporating other atmospheric features (e.g., migratory anticyclones, upper-level troughs, large convective systems), which limits the interpretation of results.

In this context, Michaelides et al. (1999) developed a Semi-Lagrangian framework for analyzing cyclone energetics, where the computational domain is movable. This approach minimizes the impact of neighboring circulations on the system’s energy dynamics by employing a regional computational domain that follows the cyclone

116 track. In the present study, we present a LEC climatology applied to cyclonic sys-
 117 tems using such a framework, as well as the first LEC climatology (considering both
 118 Eulerian and Semi-Lagrangian frameworks) for cyclones in the Southwestern Atlantic.
 119 Over 6,700 cyclones with genesis in the Southwestern Atlantic region are analyzed,
 120 and their energy cycles are divided into distinct life cycle phases: incipient, intensifica-
 121 tion, mature, and decay. This division allows for a more comprehensive understanding
 122 of the energy flows and the dynamical mechanisms acting across each phase of the
 123 cyclone’s life cycle.

124 2 Materials and methods

125 2.1 Data

126 For both the cyclone tracking and energetics computations, we employed the fifth-
 127 generation reanalysis from the European Centre for Medium-Range Weather Forecasts
 128 (ECMWF), known as ERA5 (Hersbach et al., 2020). ERA5 data are produced using
 129 the Integrated Forecasting System (IFS) Cy41r2, which assimilates a wide range of
 130 observations, including satellite and in-situ measurements. It provides global coverage
 131 of numerous atmospheric, ocean-wave, and land-surface parameters at a horizontal
 132 resolution of approximately 31 km (0.25°). In this study, we utilized data from all 37
 133 pressure levels, ranging from 1000 hPa to 1 hPa, with a temporal interval of three
 134 hours.

135 The cyclone tracks used in this study were obtained from the ”Atlantic Extratrop-
 136 ical Cyclone Tracks Database” (Gramscianinov et al., 2020). This database tracks the
 137 central relative vorticity of cyclones at the 850 hPa level (ζ_{850}) using the TRACK algo-
 138 rithm (Hodges, 1994, 1995) and the method outlined by Hoskins and Hodges (2002).
 139 This algorithm has been employed in previous studies to assess cyclone climatologies
 140 in the South Atlantic region (Gramscianinov et al., 2019, 2020; de Souza et al., 2024).
 141 The database covers the period from 1979 to 2020 and spans the entire Atlantic Ocean
 142 within the spatial domain of 15°S–55°S and 75°W–20°E. The use of ERA5, instead of
 143 other reanalysis datasets, is justified by its higher spatial resolution, which improves
 144 cyclone detection in regions with complex orography and temperature gradients, such
 145 as the SESA region (Gramscianinov et al., 2020). A detailed description of the tracking
 146 methodology can be found in Gramscianinov et al. (2020).

147 The cyclone tracking procedure employed multiple criteria to ensure accurate
 148 cyclone detection. These criteria required cyclones to have a duration of at least
 149 24 hours and a minimum displacement of 1000 km, consistent with previous South
 150 Atlantic cyclone climatologies (Sinclair, 1995; Gramscianinov et al., 2019). Systems
 151 that spent over 80% of their life cycle over continental regions were excluded from
 152 the analysis to avoid counting thermal lows and lee troughs (e.g. Crespo et al., 2021).
 153 Notably, although the TRACK algorithm’s calibration and sensitivity are focused on
 154 extratropical cyclones — the majority of systems in this region (Marrafon et al., 2022)
 155 — the methodology does not explicitly exclude subtropical or tropical cyclones.

156 To focus on the Southwestern Atlantic Ocean, only cyclones with genesis near the
 157 South American coast, specifically within the ARG, LA-PLATA, and SE-BR genesis

regions (Gramscianinov et al., 2019; de Souza et al., 2024), were included. After applying these selection criteria, the database initially comprised a total of 7931 cyclones. The spatial distribution of these genesis regions and the cyclone track density for all selected systems are presented in Figure 1. Among these 7931 cyclones, 4445 originated in ARG (56.0%), 1870 in LA-PLATA (23.6%), and 1616 in SE-BR (20.4%).

However, due to data availability issues during the download process from the ERA5 database, not all cyclones could be considered in this study, resulting in a reduced total of 6789 cyclones. These issues were related to the ERA5 API instability during the second half of 2023 and the first half of 2024, when ECMWF was migrating its data infrastructure and updating its API services. As a result, slow transfers and repeated interruptions caused incomplete or failed downloads, despite multiple attempts. This led to some cyclones being excluded from the analysis. The remaining dataset still includes a sufficiently large number of systems for robust analysis and generalization of the results. Of the 6789 cyclones, 4015 originated in ARG (59.1%), 1288 in LA-PLATA (18.9%), and 1486 in SE-BR (21.8%). The reduction corresponds to a 14.4% decrease in the number of cyclones, with region-specific reductions of 9.7% for ARG, 31.1% for LA-PLATA, and 8.0% for SE-BR.

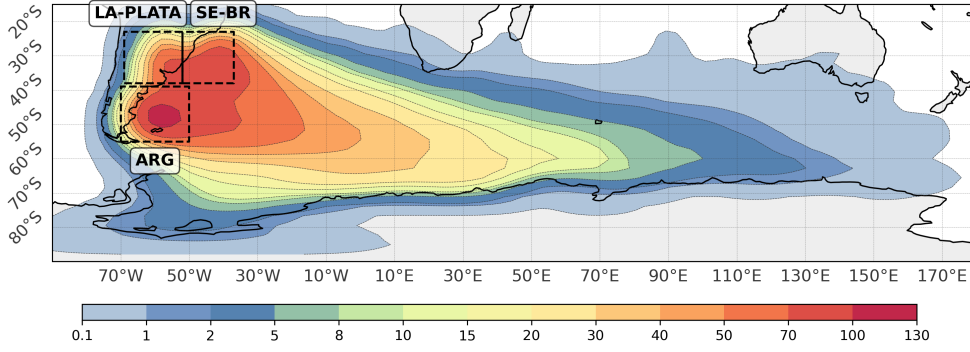


Fig. 1 Cyclone track density for all systems analyzed in this study, highlighting the cyclogenesis regions near the South American coast (ARG, LA-PLATA, and SE-BR). The track density unit is cyclonic centers per 10^6 km^2 per month.

2.2 Lorenz Energy Cycle Computation

For computing the LEC, we used the the open-source Python application LorenzCycleToolKit (de Souza et al., 2024). The energy budget equations for the zonal and eddy forms of APE and kinetic energy are then expressed as:

$$\frac{\partial A_Z}{\partial t} = BA_Z - C_Z - C_A + G_Z \quad (1)$$

$$\frac{\partial A_E}{\partial t} = BA_E - C_E + C_A + G_E \quad (2)$$

$$\frac{\partial K_Z}{\partial t} = BK_Z + C_Z - C_K + B\Phi_Z - D_Z \quad (3)$$

$$\frac{\partial K_E}{\partial t} = BK_E + C_E + C_K + B\Phi_E - D_E \quad (4)$$

179 In these equations, the atmospheric energy reservoirs are separated into zonal and
 180 eddy components of available potential energy (A_Z , A_E) and kinetic energy (K_Z , K_E).
 181 Energy conversions between reservoirs are represented by the following terms: C_A , the
 182 conversion between zonal and eddy available potential energy ($A_Z \leftrightarrow A_E$); C_E , the
 183 conversion from eddy available potential energy to eddy kinetic energy ($A_E \leftrightarrow K_E$);
 184 C_K , the barotropic conversion from eddy kinetic energy to zonal kinetic energy ($K_E \leftrightarrow$
 185 K_Z); and C_Z , the conversion from zonal available potential energy to zonal kinetic
 186 energy ($A_Z \leftrightarrow K_Z$). The generation of available potential energy (G) and dissipation of
 187 kinetic energy (D) are indicated by subscripts Z and E , such that G_Z and G_E represent
 188 the generation of zonal and eddy available potential energy, while D_Z and D_E denote
 189 the dissipation of zonal and eddy kinetic energy, respectively. The boundary flux
 190 terms, BA_Z , BA_E , BK_Z , and BK_E , represent the import/export of available potential
 191 energy and kinetic energy across the computational domain boundaries. Additionally,
 192 the terms $B\Phi_Z$ and $B\Phi_E$ appear alongside C_Z and C_E , respectively, as both arise from
 193 deriving the kinetic energy balances. According to Muench (1965), these terms are
 194 challenging to interpret physically, but indicate processes generating kinetic energy
 195 resulting from work performed at the boundaries of the computational domain. The
 196 complete mathematical formulation of these terms can be found in the Appendix.

197 In these formulations, a global reference state is used to define the APE, meaning
 198 that the computed APE represents the contribution of local APE to global energetics
 199 (Smith, 1980). As a result, it does not account for regional variability, which can
 200 introduce bias in the APE computation (see Novak and Tailleux (2018) for a thorough
 201 discussion). Despite the limitations of this methodology, the formulations by Muench
 202 (1965) and Brennan and Vincent (1980) still provide a valuable framework due to their
 203 simplicity, robustness, and ability to yield consistent, interpretable results, enabling
 204 direct analysis of the dynamic processes driving cyclones development (Dias Pinto
 205 and Rocha, 2011; de Souza et al., 2025, e.g.). Moreover, while using a local APE
 206 definition (Novak and Tailleux, 2018, e.g.) offers more precise results, it often comes
 207 with higher computational costs and does not provide the same level of direct, practical
 208 interpretability.

209 Following the methodologies of Brennan and Vincent (1980); Michaelides (1987);
 210 Veiga et al. (2008); Pezza et al. (2010); Dias Pinto and Rocha (2011), the program was
 211 set to compute the generation, dissipation and boundary pressure work terms ($B\Phi_Z$
 212 and $B\Phi_E$) as residuals, defined as:

$$RK_Z = B\Phi_Z - D_Z + \epsilon_{KZ} \quad (5)$$

$$RK_E = B\Phi_E - D_E + \epsilon_{KE} \quad (6)$$

$$RG_Z = G_Z + \epsilon_{GZ} \quad (7)$$

$$RG_E = G_E + \epsilon_{GE} \quad (8)$$

Where ϵ account for numerical errors in the computation procedures. The set of budget equations becomes, then:

$$\frac{\partial A_Z}{\partial t} = -C_A - C_Z + RG_Z + BA_Z \quad (9)$$

$$\frac{\partial A_E}{\partial t} = C_A - C_E + RG_E + BA_E \quad (10)$$

$$\frac{\partial K_Z}{\partial t} = C_K + C_Z + BK_Z + RK_Z \quad (11)$$

$$\frac{\partial K_E}{\partial t} = -C_K + C_E + BK_E + RK_E \quad (12)$$

A complete depiction of the LEC, with arrows indicating positive energy fluxes, is presented in Figure 2. This figure also highlights three primary energetic pathways (baroclinic instability, barotropic conversion, and latent heat release) which will be discussed throughout the text.

Here, we used a Semi-Lagrangian framework (Michaelides et al., 1999), aiming to minimize interactions with other non-related circulations while capturing the main structure of the cyclone. A $15^\circ \times 15^\circ$ computational domain centered at the cyclone’s central position, obtained from the TRACK database, was created for each time step. Given the impracticality of manually selecting an appropriate domain size for each cyclone in the dataset, a fixed size was employed. The choice of a $15^\circ \times 15^\circ$ computational domain is justified as it is large enough to capture the effective radius of most cyclonic systems (Rudeva and Gulev, 2007). The effective cyclone radius is defined as a measure of cyclone size, determined by establishing a coordinate system centered on the cyclone and measuring the distance at which the radial pressure gradient first falls to zero. This domain size also is large enough for accommodating the cyclone’s synoptic structure (e.g. Gramscianinov et al., 2019).

2.3 Analysis Methods

A key challenge in computing the LEC for large datasets lies in the variable life durations of cyclones. Averaging energy values across an entire life cycle can obscure distinct dynamical processes tied to different stages of cyclone development, while technical limitations exist in dissecting the life cycle into distinct periods. For example, Black and Pezza (2013) averaged cyclone energetics over periods of 48 hours before explosive cyclogenesis, during explosive deepening, and for 24 and 72 hours after it. However, cyclone life cycles can range from less than 24 hours to over 10 days (Trigo, 2006; Reboita et al., 2010; Gramscianinov et al., 2019), presenting significant physical limitations to such approaches.

To address these issues, we employed Cyclophaser, an open-source Python package designed to detect cyclone life cycle phases (de Souza et al., 2025). This program uses time series of relative vorticity at the system’s central position and its first derivative to identify intensification, mature, and decay phases based on peaks and valleys in

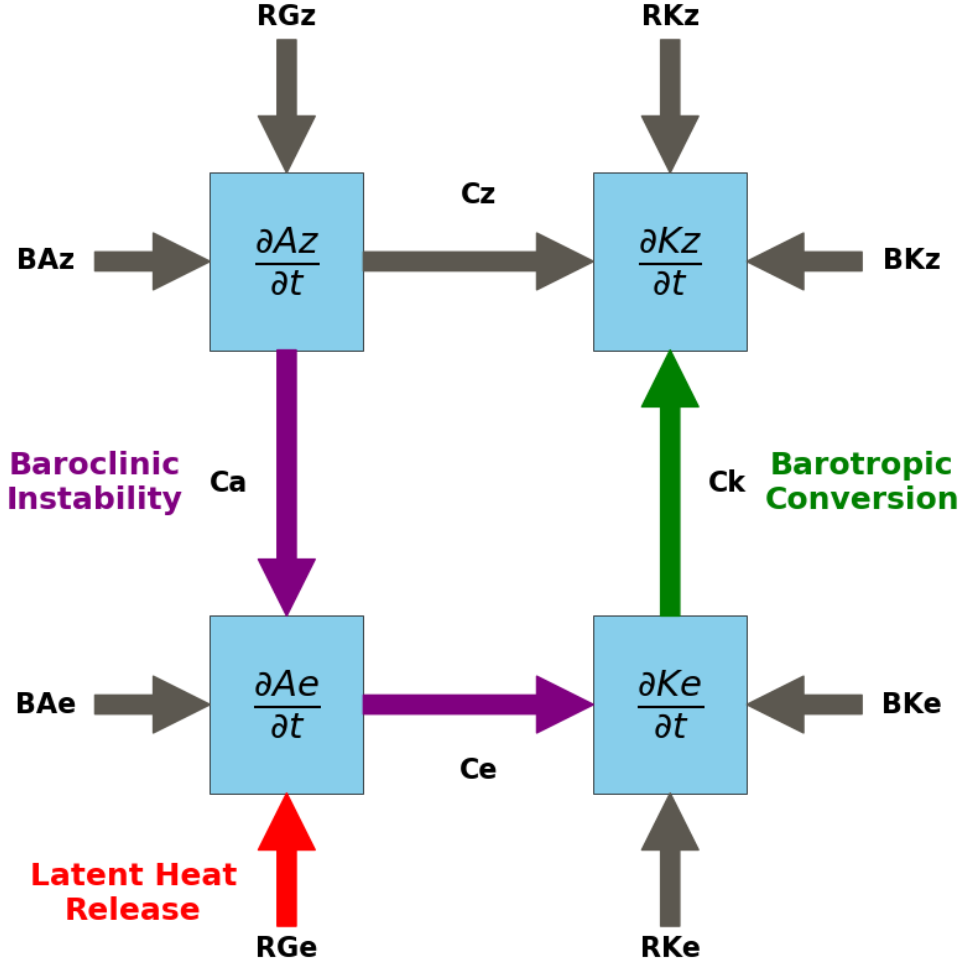


Fig. 2 Representation of the Lorenz Energy Cycle (LEC), with arrows denoting positive energy fluxes. The figure also indicates three main energetic pathways: baroclinic instability (purple), barotropic conversion (green), and latent heat release (red), which will be addressed in detail in the following sections.

the vorticity and its derivative. In this study, we adopted the same life cycle detection approach as de Souza et al. (2024). After computing the LEC for each system, Cyclophaser was used to identify the life cycle phases for all analyzed cyclones, followed by the computation of mean LEC values for each phase. This approach facilitates the investigation of dynamical mechanisms specific to each development phase. For example, distinct energy fluxes are expected to dominate during the intensification and decay phases, particularly near the cyclone center. As shown by de Souza et al. (2024), approximately 60% of the analyzed cyclones follow a classical life cycle, consisting of incipient, intensification, mature, and decay phases, while over 95% display at

least one intensification phase. A comprehensive description of the detection methodology, as well as spatial distributions and phase-specific statistics such as duration, displacement, speed, and intensity, can be found in de Souza et al. (2024).

To understand the dominant LEC variability patterns within the TRACK dataset, we performed an Empirical Orthogonal Function (EOF) analysis (Fukuoka, 1951; Lorenz, 1956) using the Python open-source library pyEOF (Zheng, 2021). This analysis reduces the dimensionality of the dataset, retaining the most significant variability, and is particularly useful for uncovering underlying structures and patterns in complex environmental data. Typically, each EOF represents a spatial pattern, while the associated time series, or principal component (PC), describes the temporal evolution of that pattern. However, in this study, each EOF reflects a mode of variability derived from all LEC terms, using their average values computed separately for each cyclone life cycle phase (incipient, intensification, mature, and decay). Consequently, the PCs represent the variation across individual cyclones rather than temporal evolution, and therefore are not displayed individually, as they do not depict any meaningful temporal or spatial feature. Performing EOF analyses separately for each life cycle phase enabled a detailed investigation of the variability in cyclone energetics across distinct stages of cyclone development, as well as throughout the entire energy cycle.

To associate cyclones with predominant EOFs, we first project each cyclone’s energetics onto the PCs obtained from an EOF analysis. This allows us to represent each system in terms of its contribution to the dominant modes of variability. Next, we classify cyclones into EOF(+) and EOF(-) groups, identifying systems where at least one PC reaches extreme values. Specifically, EOF(+) corresponds to cyclones where at least one PC exceeds the 90th percentile (q90), indicating a strong positive projection onto a specific mode. Meanwhile, EOF(-) are cyclones for which at least one PC is below the 10th percentile (q10), indicating strong negative projection onto a specific mode. For each cyclone meeting these criteria, we determine its predominant EOF as the one corresponding to the PC with the highest absolute value. This ensures that each system is classified based on the mode that most strongly characterizes its structure and dynamics.

To determine the LEC patterns of the most intense systems, we first selected only the cyclones in which the maximum central vorticity at 850 hPa exceeded the 90th percentile of the dataset. Subsequently, we applied the K-Means algorithm to the PCs of these intense cyclones to investigate whether distinct energetic characteristics could be identified among them. This clustering analysis was not performed on all cyclones, as sensitivity tests indicated that applying it to the full dataset resulted in groups that differed mainly in intensity rather than exhibiting distinct energetic behaviors (not shown); thus, intensity-based selection was necessary.

K-Means is an unsupervised learning algorithm that partitions data into K clusters by minimizing intra-cluster variance while maximizing separation between groups based on sample similarity (MacQueen et al., 1967; Hartigan and Wong, 1979). The optimal number of clusters was determined using the Elbow Method, which identifies the most suitable number of clusters by plotting the within-cluster sum of squares for different values of K and locating the “elbow point,” where the rate of decrease slows, indicating a balance between model complexity and performance. For this analysis, we

employed the K-Means implementation from the `scikit-learn` Python package (Hao and Ho, 2019) and used the `yellowbrick` package for the Elbow Method (Bengfort and Bilbro, 2019).

3 Results

3.1 Climatological Features

The exploratory statistical metrics for all LEC terms, presented as averages across the entire cyclone lifecycle, are shown in Table 1, while their probability density functions (PDFs) are provided in Figure 3. Notably, all terms related to the zonal jets (K_Z , BK_Z , and $\frac{\partial K_Z}{\partial t}$) frequently exhibit statistical metrics one order of magnitude higher than their eddy counterparts within the same group (K_E , BK_E , and $\frac{\partial K_E}{\partial t}$), indicating significantly greater energy amount concentrated on the jet streams. Although the energy budgets were computed with the generation and dissipation terms calculated as residuals, the generation terms can be directly computed using ERA5 data. Therefore, their probability density functions (PDFs) are also shown for a more physically based analysis (Figure 3e). Furthermore, the comparison between the directly computed generation values and those estimated by residual computation provides a useful metric for evaluating the accumulation of errors in LEC computation procedure. The dissipation terms were not directly computed in the present study.

All the energy terms (K_Z , A_Z , A_E , and K_E , Figure 3a) exhibit right-skewed distributions. Among these, A_Z shows the largest variability, as reflected in its long-tail distribution, standard deviation (std), interquartile range (IQR), and range (defined as the difference between maximum and minimum values), compared to A_E and K_E , peaking at approximately $4 \times 10^5 J m^{-2}$. Conversely, A_E presents the lowest variability, peaking near $1 \times 10^5 J m^{-2}$, closer to its mean value. The kinetic energy terms, K_Z and K_E , display similar distributions, with K_Z peaking near $20 \times 10^5 J m^{-2}$ and K_E peaking near $2 \times 10^5 J m^{-2}$.

For the conversion terms, C_Z , C_K , and C_E exhibit high variability, in contrast to C_A . The former terms display long-tail distributions, peaking near zero, -1 , and $2 W m^{-2}$, respectively, while C_A presents a narrow distribution with a sharp peak near its mean value, close to zero (Figure 3b). The C_Z probability density function (PDF), along with the mean and quantile values, and its mean value being close to the median, indicate an overall tendency for both $A_Z \rightarrow K_Z$ and $K_Z \rightarrow A_Z$ conversions. However, the positive mean and median values suggest a predominant $A_Z \rightarrow K_Z$ pathway. For C_A and C_E , the metrics presented in Table 1 indicate a consistent tendency for positive conversions, corresponding to $A_Z \rightarrow A_E \rightarrow K_E$ (baroclinic chain), but with more modest $A_Z \rightarrow A_E$ conversions than $A_E \rightarrow K_E$. In the case of the C_K term (barotropic conversion term), the metrics indicate a predominant negative conversion, i.e., $K_Z \rightarrow K_E$, although the positive Q75 value suggests the occurrence of events where $K_E \rightarrow K_Z$ conversions also take place.

For the boundary terms, BA_E and BK_Z exhibit similar distributions, as do BA_Z and BK_E (Figure 3c). The terms BA_E and BK_E display narrow distributions, peaking near zero, whereas BA_Z and BK_Z show nearly symmetrical long-tail distributions. Although for all four terms, both positive (influx) and negative (outflux) energy fluxes

Table 1 Summary Statistics of Lorenz Energetics Components, computed as averages across the entire cyclone lifecycle: mean, median, standard deviation (std), 25th percentile (Q25), 75th percentile (Q75), interquantile range (IQR), and range. The IQR measures the range within which the central 50% of the values fall, while the range is computed as the difference between the maximum and minimum values. The units for the energy terms (A_Z , A_E , K_Z , and K_E) are $10^5 J m^{-2}$ and $W m^{-2}$ for the remaining terms.

Term	Mean	Median	Std Dev	Q25	Q75	IQR	Range
A_Z	5.55	4.68	3.71	2.77	7.49	4.72	36.46
A_E	1.62	1.24	1.20	0.77	2.09	1.32	11.07
K_Z	28.55	26.19	15.10	17.34	37.12	19.78	114.55
K_E	3.70	2.95	2.62	1.92	4.63	2.71	24.81
C_Z	0.52	0.38	4.85	-1.96	2.92	4.89	86.70
C_A	0.93	0.46	1.57	0.02	1.44	1.41	19.78
C_K	-3.56	-1.63	9.51	-5.77	0.47	6.24	206.43
C_E	3.84	2.47	4.92	0.63	5.84	5.21	54.74
BA_Z	3.54	2.03	7.67	-0.67	6.67	7.34	175.05
BA_E	0.58	0.16	4.40	-1.13	2.02	3.15	75.72
BK_Z	-7.93	-5.53	31.75	-23.75	7.83	31.58	445.63
BK_E	0.47	0.08	8.59	-2.73	3.22	5.95	146.87
$B\Phi_Z$	63.87	49.25	128.05	-9.12	132.35	141.47	1419.08
$B\Phi_E$	39.66	31.19	126.50	-28.84	109.47	138.32	1353.99
G_Z	-0.31	-0.17	2.66	-1.39	0.81	2.21	68.74
G_E	1.17	0.56	3.14	-0.26	2.21	2.46	58.39
$\frac{\partial A_Z}{\partial t}$	-0.07	-0.14	4.46	-2.04	1.68	3.71	106.39
$\frac{\partial A_E}{\partial t}$	-0.23	-0.10	1.92	-0.85	0.51	1.35	48.19
$\frac{\partial K_Z}{\partial t}$	1.59	0.75	13.38	-5.33	8.15	13.48	251.24
$\frac{\partial K_E}{\partial t}$	0.28	0.12	3.18	-1.13	1.58	2.71	61.50
RG_Z	-2.17	-1.00	7.60	-5.22	1.56	6.78	220.06
RK_Z	12.56	8.69	40.49	-8.68	32.71	41.39	561.24
RGE	2.10	1.20	5.15	-0.40	4.21	4.61	97.25
RKE	-7.59	-4.63	10.62	-11.48	-1.04	10.43	138.42

occur, as indicated by their negative Q25 and positive Q75 values, the peak near zero for BA_E and BK_Z suggests that boundary energy fluxes are typically low in most cases. In contrast, for BA_Z , the peak near $2 W m^{-2}$ indicates an overall tendency for energy influx, while for BK_E , the peak near $-2 W m^{-2}$ points to a predominant tendency for energy outflux. Meanwhile, the boundary pressure work terms ($B\Phi_Z$ and $B\Phi_E$) exhibit significantly higher values compared to the other boundary terms, with both presenting nearly symmetric distributions (Figure 3d). These terms show tail distributions exceeding $\pm 200 W m^{-2}$, indicating substantial variability. The physical interpretation of these terms is discussed in Section 4.1.

Overall, both generation terms (G_Z and G_E) present nearly symmetrical distributions centered near zero (Figure 3e), suggesting that in most cases, either the zonally averaged diabatic heating (G_Z) and the zonal deviations (G_E) are low, or the atmospheric stability is high. However, there are instances where this behavior is amplified ($G < 0$) or reversed ($G > 0$). In contrast, the generation residual terms (RG_Z and RG_E) display distinct characteristics. The RG_Z term is left-skewed, with a long-tail distribution and higher variability compared to G_Z , as indicated by its lower Q25

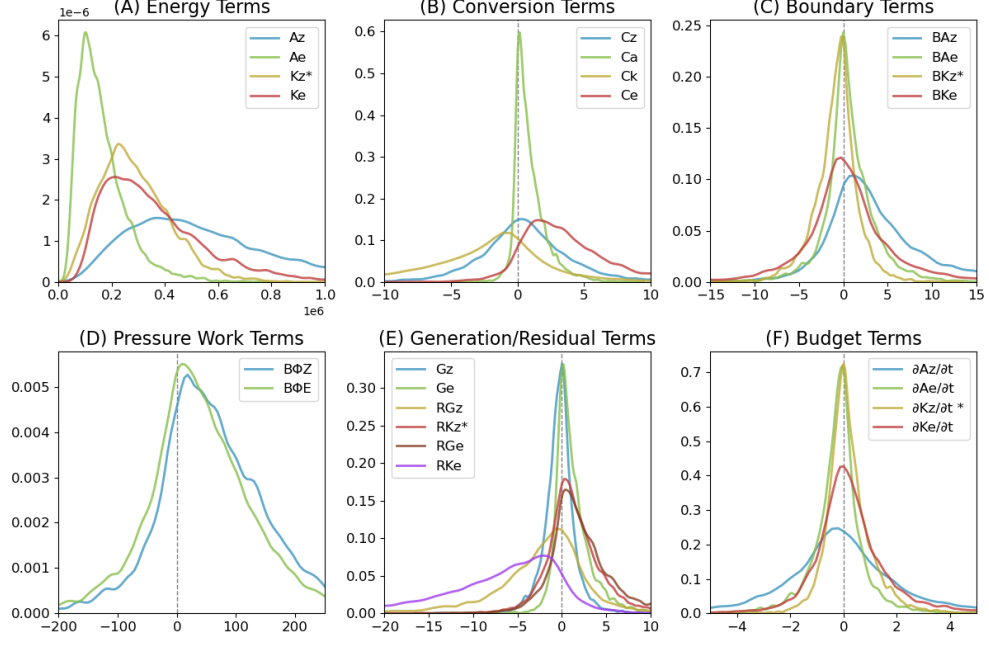


Fig. 3 Probability density function (PDF) plots for distinct Lorenz Energetics terms, computed as averages across the entire cyclone lifecycle: (A) energy, (B) conversion, (C) boundary, (D) pressure work, (E) generation and residual, and (F) budget terms. The x-axis represents the energy values, while the y-axis represents density counts. The units for the energy terms (A_Z , A_E , K_Z , and K_E) are in $10^5 J m^{-2}$, and in $W m^{-2}$ for the remaining terms. Terms related to K_Z are divided by 10 (*) to account for their order of magnitude difference, which would otherwise distort the visualization.

and higher Q75 and IQR values (Table 1). Additionally, RG_Z exhibits more negative mean and median values than G_Z , suggesting a bias toward processes such as diabatic cooling at lower latitudes and/or heat distribution mechanisms that reduce zonal temperature gradients, such as cyclonic activity. On the other hand, RG_E is more symmetrical than RG_Z , though it still shows higher variability compared to G_E , as evidenced by its lower Q25 and higher Q75 and IQR values. Moreover, RG_E exhibits higher mean and median values than G_E , indicating a bias toward overestimating the eddy effects on latent heat release and meridional temperature gradients. Therefore, the residuals suggest that the computed LEC increases the contribution of eddy motions to the atmospheric energy cycle through enhanced meridional heat transport, reducing zonal temperature gradients and enhancing convective activity within cyclone frontal structures.

Similar to the generation residual terms, each dissipation residual term displays distinct distributions (Figure 3e). The PDF for RK_Z mirrors that of RG_E , showing modest variability. Its negative Q25 values indicate instances of net dissipation of K_Z . However, the high positive mean, median, Q75, and IQR values suggest that in most cases, there is a net increase of K_Z related to this term, possibly due to the high $B\Phi_Z$ value. In contrast, RK_E shows high variability with a left-skewed, long-tail

376 distribution. Both its Q25 and Q75 are negative, indicating that dissipation of K_E
377 frequently occurs.

378 3.2 Mean Energy Values Across Life Cycle Phases

379 The use of the CycloPhaser program allowed for the application of an objective cri-
380 terion to dissect the cyclones into distinct life cycle phases, enabling an investigation
381 of their energy cycles across these phases (Figure 4). Our analysis revealed that the
382 mean energy flow directions rarely change across phases, although the magnitude of
383 each term varies. However, the high standard deviation values indicate that energy
384 fluxes frequently deviate from their mean direction.

385 The A_Z budget term exhibits mean positive values during the incipient phase,
386 which turn negative during the intensification and mature phases, becoming positive
387 again during the decay phase. The mean K_Z budget values are positive throughout
388 all phases except during the mature phase. In contrast, the A_E budget remains neg-
389 ative across the entire lifecycle, while the K_E budget is positive during the incipient
390 and intensification phases but turns negative during the mature and decay phases.
391 However, it is important to note that the large variability observed in these terms indi-
392 cates that numerous individual cases deviate significantly from these mean behaviors,
393 including instances of opposite signs or substantially greater magnitudes.

394 Across the different cyclone phases, the mean behavior suggests that both baro-
395 clinic and barotropic conversions remain active, continuously providing energy to the
396 eddies, while the adiabatic contribution from the G_E term is variable throughout the
397 lifecycle. There is a marked enhancement of baroclinic conversions from the incipi-
398 ent to intensification phase, which then decrease in magnitude during the mature and
399 decay phases. Conversely, barotropic conversion peaks during the mature phase, sur-
400 prisingly with a higher magnitude than the $A_E \rightarrow K_E$ conversion. The behavior of
401 the baroclinic chain is mirrored by the G_E term, which begins with negative values
402 and, during the intensification phase, reaches a higher magnitude than the C_A term.
403 The large variability observed in these energy conversion terms indicates that multiple
404 cyclone configurations likely exist, where either baroclinic or barotropic conversions
405 dominate, or where both pathways coexist with varying intensities. Furthermore, the
406 variability of the G_E term suggests that, in some systems, adiabatic heating plays a
407 significant role in cyclonic development, while in others, diabatic cooling hinders the
408 development. The G_Z term remains negative throughout the entire life cycle, with
409 progressively decreasing values.

410 Throughout the life cycle, the mean values indicate imports of A_Z , which decrease
411 in the mature phase but rise again during the decay phase. The mean BA_E values
412 exhibit a bimodal behavior, being positive during the incipient and intensification
413 phases but turning negative during the mature and decay phases, though with negli-
414 gible mean values in the latter. However, the large variability observed suggests that
415 for individual cyclones, imports and exports of A_Z and A_E can differ substantially
416 from these mean patterns, with some systems potentially exhibiting more pronounced
417 or negligible boundary flux contributions.

418 Across all phases, the RK_Z term stands out with the highest mean values, also
419 displaying the greatest variability, as indicated by the high standard deviation values.

420 This could be influenced by the $B\Phi Z$ term, as mentioned in the previous section. The
 421 BK_Z term also presents high mean values and variability across all phases, suggesting
 422 a compensatory effect for the excess energy from the RK_Z term. Lastly, the mean RK_E
 423 values are negative across all phases, peaking during the mature phase, indicating
 424 significant dissipation in this phase and presenting similar values during the incipient
 425 and decay phases.

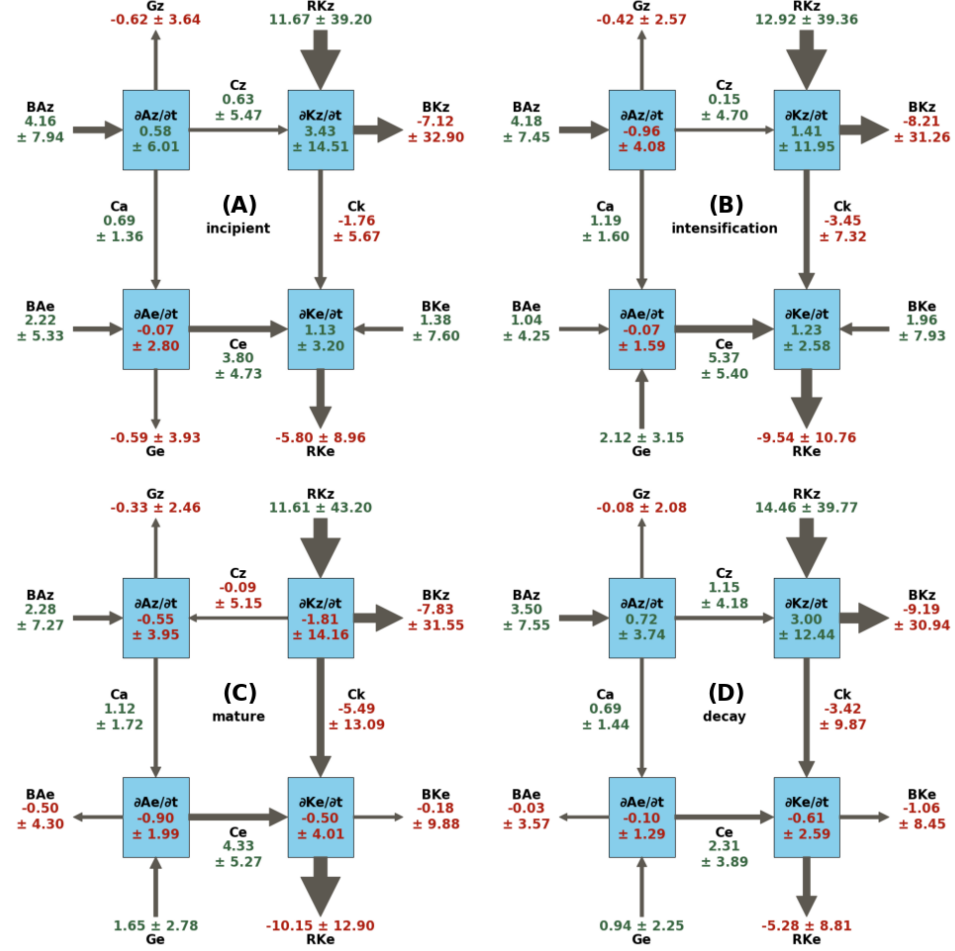


Fig. 4 Mean values and standard deviation of the limited-area Lorenz Energy Cycle (LEC) terms for each life cycle phase : incipient (A), intensification (B), mature (C), and decay (D). Each box represents an energy component ($J m^{-2}$), with arrows showing the direction of energy flow ($W m^{-2}$). The numbers adjacent to the arrows indicate the magnitude and direction of the energy flux, with green indicating positive values and red indicating negative values

3.3 Empirical Orthogonal Function Analysis

To better characterize the substantial variability observed in the LEC terms, we performed an Empirical Orthogonal Function (EOF) analysis to identify distinct energetic configurations throughout the cyclone lifecycle. The first EOF accounts for 28.3% of the total variance, followed by the second and third EOFs with 11.0% and 10.9%, respectively. The fourth to eighth EOFs contribute progressively less (8.2%, 7.4%, 5.9%, 5.2%, and 4.4%), with the first four modes explaining 58.4% of the total variance and the first eight reaching 81.3%. These results highlight the dominant patterns of variability, with diminishing contributions beyond the initial modes. This study focuses on the first four EOFs. Although EOFs can be interpreted in terms of both positive and negative contributions, we limit our analysis to the positive phase for simplicity.

Each cyclone can be described as a linear combination of the EOFs, with the corresponding principal components (PCs) indicating how strongly each mode contributes to the system's energetic structure. Consequently, the importance of a given EOF varies from system to system. The energy fluxes associated with each EOF represent deviations from the climatological mean (Figure 4), either reinforcing or weakening specific energy pathways. In this way, each EOF reflects the amplification or attenuation of a characteristic energy transfer pattern within the LEC. In section 3.4, we examine cyclones that project strongly onto each EOF individually.

Figure 5 illustrates the Lorenz Energy Cycle (LEC) terms associated with EOF 1. Across all life cycle phases, there is a consistent enhancement of moist baroclinic conversions, characterized by the positive values of the $A_Z \rightarrow A_E \rightarrow K_E$ conversions, in conjunction with an enhancement of the G_E term. Furthermore, there is an increase in the $K_Z \rightarrow K_E$ conversion (C_K becomes more negative), particularly during the mature and decay phases. These variations largely reinforce the mean behavior observed across the cyclone's life cycle. In addition, A_Z imports are enhanced, while a negative tendency is observed in its budget and generation terms. Conversely, the K_Z boundary, budget, and residual terms show a positive tendency. Lastly, the C_Z term presents a weak positive signal during the incipient and decay phases, and a negative tendency during the intensification and mature phases.

During the incipient (Figure 6A) and intensification phases (Figure 6B), EOF 2 displays an overall weakening of the C_A term, in contrast to EOF 1. Additionally, there is a reduction in barotropic conversions, indicating a $K_E \rightarrow K_Z$ tendency, alongside a weakening of K_E imports. This reduction is compensated by an enhancement in A_E imports, which appears to be the primary mechanism driving the increase in the C_E term. In the mature phase (Figure 6C), the signal for A_E imports reverses in sign, and an enhancement of the moist baroclinic chain occurs, accompanied by a slight increase in $K_Z \rightarrow K_E$ conversions and a more pronounced increase in K_E imports. During the decay phase (Figure 6D), both the moist baroclinic chain and K_Z imports show a negative tendency. However, the enhanced barotropic conversions, coupled with a weakening of dissipation (positive tendency for RK_E), result in a slight yet positive tendency in K_E , suggesting a slower dissipation process.

For EOF 3 (Figure 7), the role of the moist baroclinic chain diminishes in eddy development. This is evident from the weakening of the C_E and G_E terms across the

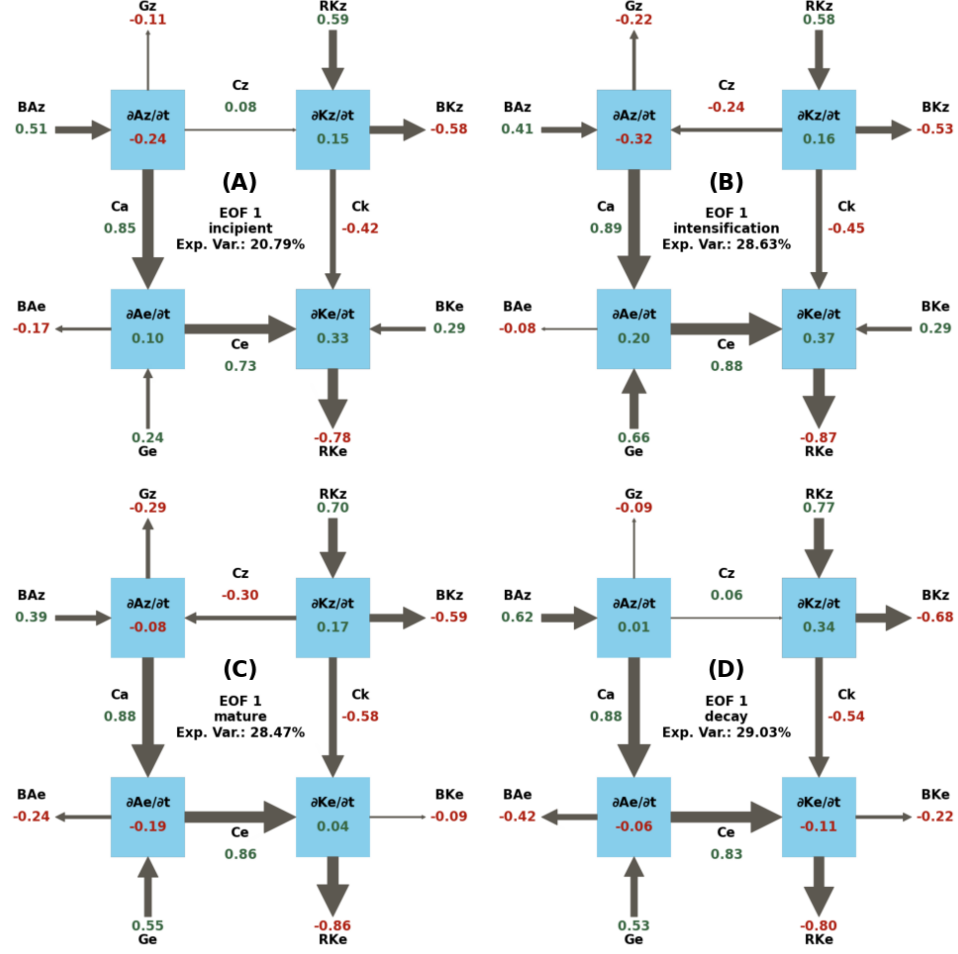


Fig. 5 Lorenz Energy Cycle (LEC) terms for the first Empirical Orthogonal Function (EOF 1) across different life cycle phases: (A) incipient, (B) intensification, (C) mature, and (D) decay.

incipient (Figure 7A), intensification (Figure 7B), and mature (Figure 7C) phases, although the C_A term shows a slight enhancement during these phases. As a result, we can expect a weaker development for the incipient phase, indicated by the reduced K_E budget. However, during the intensification and mature phases, the dominant source of energy shifts to barotropic conversions. During the decay phase (Figure 7D), the marginal enhancement of the C_E term is driven by a slight increase in the G_E term and, more importantly, by an enhancement of A_E imports. Although this works in conjunction with increased K_E imports, the simultaneous enhancement of $K_E \rightarrow K_Z$ conversions leads to the dissipation of eddies.

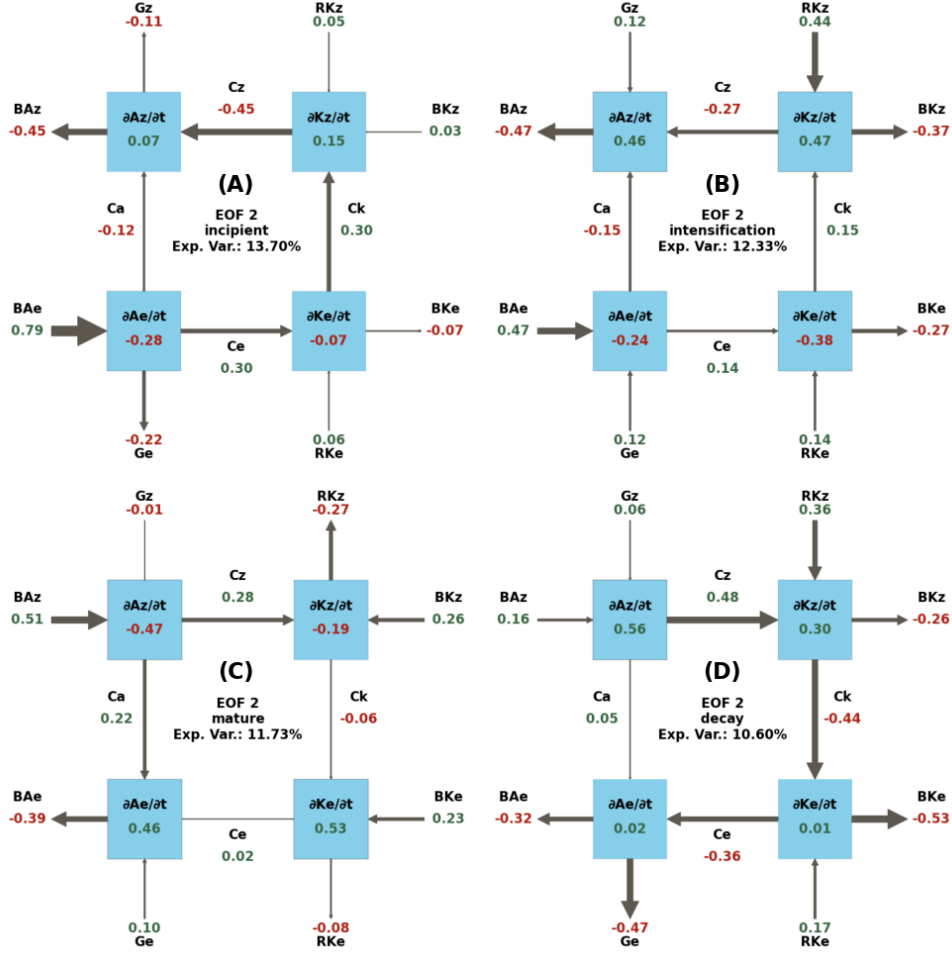


Fig. 6 Lorenz Energy Cycle (LEC) terms for the second Empirical Orthogonal Function (EOF 2) across different life cycle phases: (A) incipient, (B) intensification, (C) mature, and (D) decay.

During the incipient phase (Figure 8A) of EOF 4, the moist baroclinic chain weakens, as do the K_E imports, while the barotropic conversions are enhanced. As the system progresses to the intensification phase (Figure 8B), the barotropic conversion signal becomes neutral, and the weakening of the baroclinic chain lessens, accompanied by a strengthening of A_E imports. In the mature phase (Figure 8C), both the baroclinic chain and the A_E and K_E imports are slightly enhanced. However, the barotropic conversions reverse, signaling $K_E \rightarrow K_Z$ conversions, indicating a transfer of energy from eddy kinetic energy to zonal kinetic energy. In the decay phase (Figure 8D), the signal of baroclinic conversions returns to its initial weakened state and A_E imports are reduced, while K_E are enhanced. Although the $K_E \rightarrow K_Z$ conversions

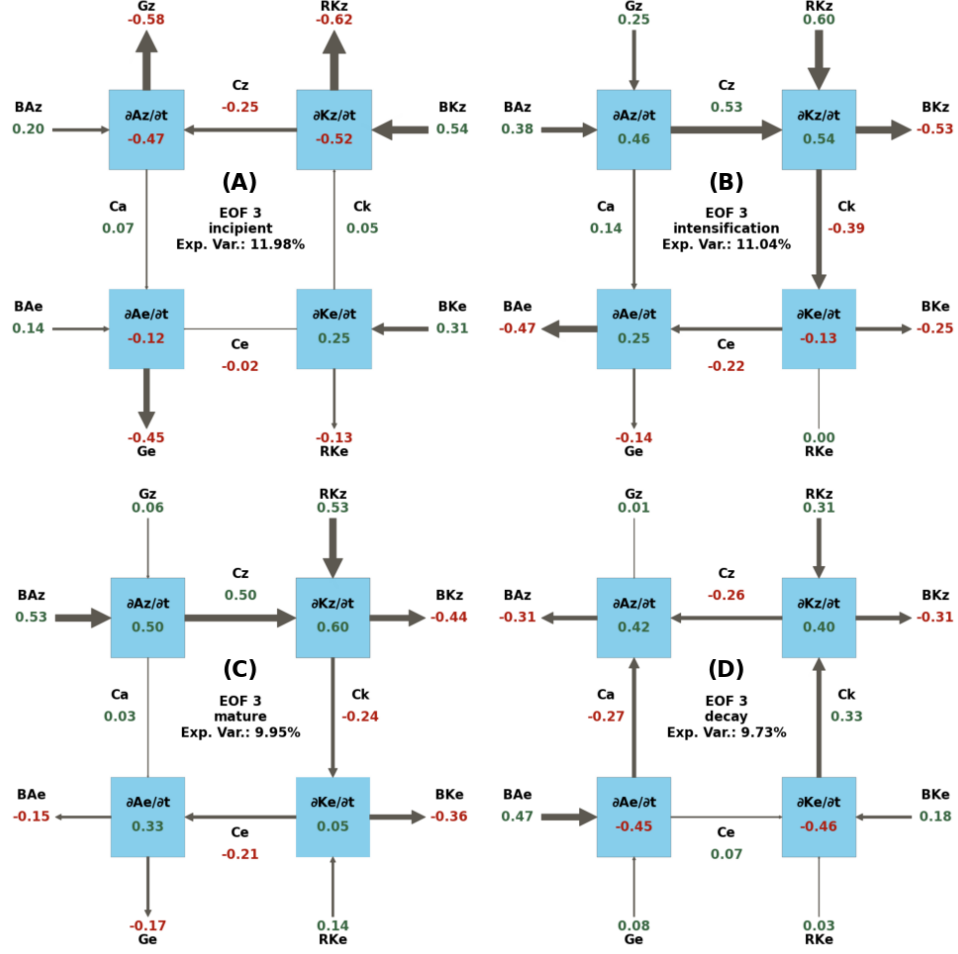


Fig. 7 Lorenz Energy Cycle (LEC) terms for the third Empirical Orthogonal Function (EOF 3) across different life cycle phases: (A) incipient, (B) intensification, (C) mature, and (D) decay.

are enhanced, they are counterbalanced by the K_E imports, leading to a slower eddy dissipation (higher tendency for K_E the budget).

Here we present a summary of the energy pathways that were enhanced for each EOF, indicating the increased contribution to cyclone development (i.e., K_E increases). During EOF1, both the moist baroclinic and barotropic chains are enhanced, with increased imports of K_E during the incipient and intensification phases. For EOF2, cyclone development is characterized by the enhancement of the $BA_E \rightarrow A_E \rightarrow K_E$ chain during the incipient and intensification phases, followed by an increase in K_E imports during the mature phase. For EOF3, during the incipient phase, there is an enhancement of K_E imports, which is followed by an increase in barotropic conversions

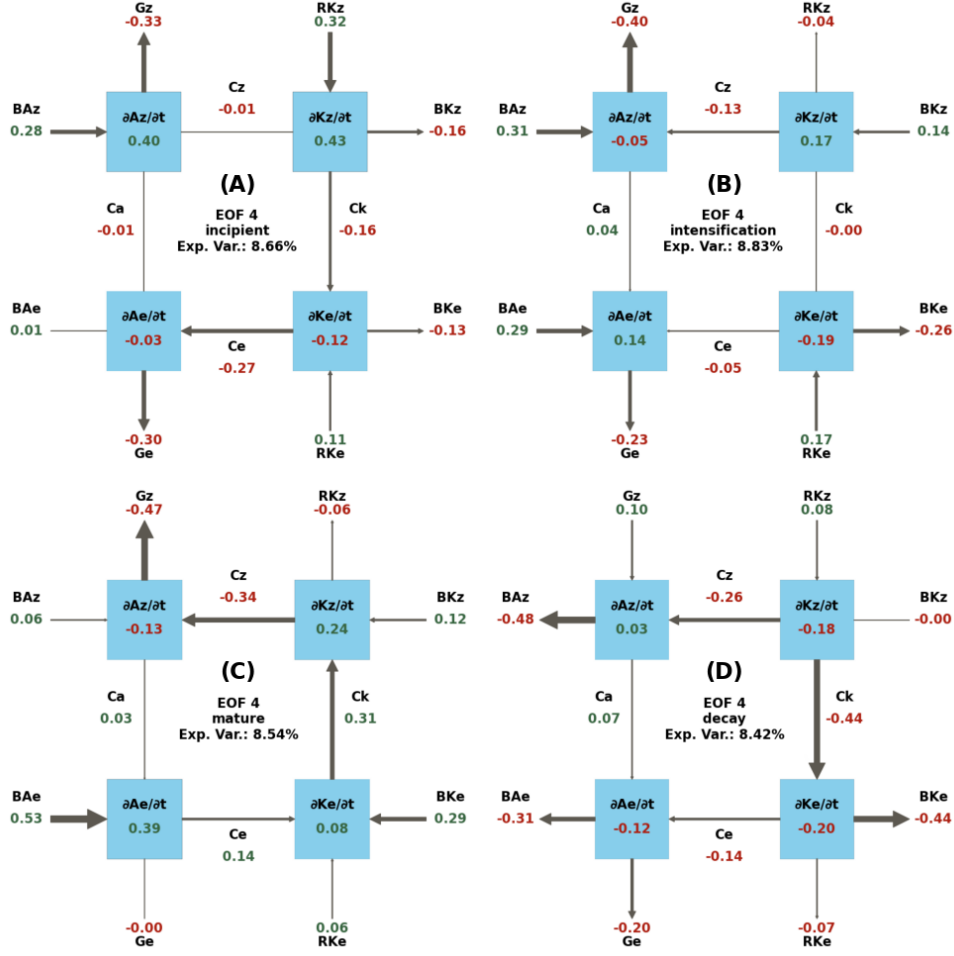


Fig. 8 Lorenz Energy Cycle (LEC) terms for the fourth Empirical Orthogonal Function (EOF 4) across different life cycle phases: (A) incipient, (B) intensification, (C) mature, and (D) decay.

during the intensification and mature phases. For EOF4, barotropic conversions are enhanced during the incipient phase, with nearly neutral baroclinic and barotropic conversions during intensification, and an enhanced baroclinic chain along with K_E imports during the mature phase. During cyclone decay, EOF1 shows an enhancement in dissipation, EOF2 and EOF4 present an enhancement in exports of K_E , and EOF3 exhibits an increase in $K_E \rightarrow K_Z$ conversions.

3.4 Systems Statistics

In this section, as the characteristics of the systems associated with each EOF are analyzed, the EOF signal becomes relevant, necessitating a distinction between systems

509 related to positive EOF signals — EOF(+) — and negative EOF signals — EOF(-),
 510 respectively. EOF1 accounts for the largest number of cyclones among the first four
 511 EOFs for both EOF(+) and EOF(-). For EOF(+), it is followed by EOF2, EOF3,
 512 and EOF4, while for EOF(-), it is followed by EOF3, EOF2, and EOF4, respectively
 513 (Figure S1a). The track densities for the cyclones associated with EOF(+) are pre-
 514 sented in Figure 9, while those for EOF(-) are shown in Figure 10. For EOF1(+),
 515 the track density maximum extends from SE-BR and LA-PLATA toward the ARG
 516 region, highlighting the significant contribution of systems originating in the former
 517 regions compared to the latter, as also indicated in Figure 11a. In contrast, for the
 518 remaining EOFs(+), the track density maximum is located near the ARG region, as
 519 most systems originate there. An exception is observed in EOF3(+), where the track
 520 density maximum extends northeastward due to the increased contribution of SE-BR
 521 systems to this EOF.

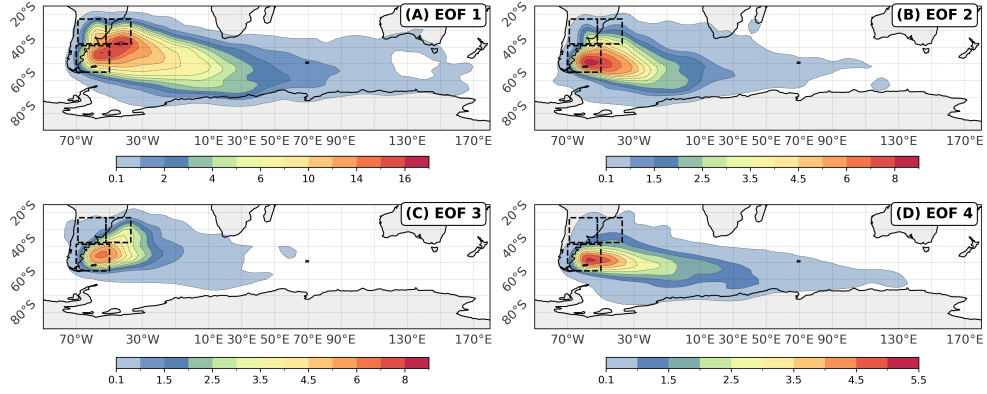


Fig. 9 Cyclone track density for the systems associated with EOFs(+): (A) EOF1, (B) EOF2, (C) EOF3, and (D) EOF4. The track density unit is cyclones per 10^6 km² per month. The dashed rectangles mark the genesis regions shown in Figure 1.

522 Meanwhile, EOFs(-) exhibit a more variable behavior. EOF1(-) displays two track
 523 density maxima: one near SE-BR and another near ARG, as fewer systems originate
 524 from LA-PLATA for this EOF (Figure 11c). EOF2(-) is predominantly influenced by
 525 ARG systems, whereas EOF3(-) shows an increased contribution from LA-PLATA
 526 systems, with a primary track density maximum near ARG and a secondary maximum
 527 over the La Plata River mouth. Lastly, EOF4(-) presents a track density maximum
 528 between LA-PLATA and SE-BR, reflecting the increased relative contribution of
 529 systems from these regions to this EOF.

530 Despite these regional differences in track density maxima, all EOFs exhibit a
 531 common pattern of cyclone tracks extending southeastward across the South Atlantic.
 532 Some systems display exceptional mobility, reaching as far as 150°E. This behavior
 533 aligns with the typical lifecycle of cyclonic systems originating near the South American
 534 coast, where cyclones generally develop near the coastal region, mature as they

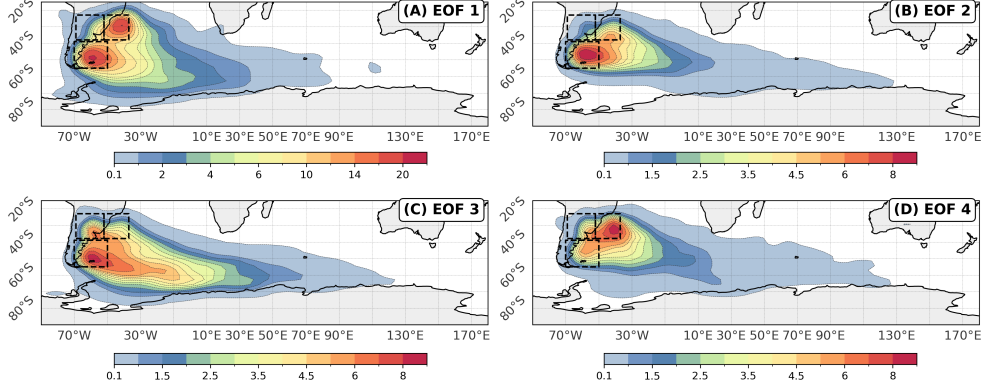


Fig. 10 Cyclone track density for the systems associated to EOFs(-): (A) EOF1, (B) EOF2, (C) EOF3 and (D) EOF4. The track density unit is cyclonic centers per 10^6 km^2 per month. The track density unit is cyclones per 10^6 km^2 per month. The dashed rectangles mark the genesis regions shown in Figure 1.

propagate southeastward, and decay closer to the Antarctic region (de Souza et al., 2024).

As shown in Figure 11b, EOF1(+) and EOF4(+) systems predominantly originate during JJA, while EOF2(+) and EOF3(+) genesis events are more evenly distributed across the seasons. For EOFs(-), EOF1(-) systems occur mainly during DJF, whereas EOF4(-) systems are more frequent during DJF and MAM. In contrast, EOF2(-) and EOF3(-) systems are predominantly observed during JJA and SON (Figure 11d). The seasonal distribution of EOF2(+) and EOF3(+) systems aligns with the expected behavior, as ARG systems are well-distributed throughout the year (Gramscianinov et al., 2019; Crespo et al., 2021). However, for the remaining EOFs, the observed behavior suggests that seasonal variations are linked to changes in the systems' energetics.

3.5 Groups of Intense Systems

While the previous sections examined the LEC for all cyclonic systems in the South Atlantic — analyzing both the mean behavior and its associated variability through EOF analysis — this section focuses on the energetic groups associated with the most intense cyclones in the dataset. The K-Means algorithm was applied to the first eight PCs of the selected cyclones, identifying five distinct LEC groups, as determined by the Elbow Method. Following the cluster identification analysis, the energetic characteristics of the systems were reconstructed, with the mean behavior for each group represented in Figure 12.

Comparing the energy fluxes of the clusters with the climatological mean computed across all cyclones provides insight into the mechanisms that distinguish these systems as the most intense (Figure 12). Cluster 1 exhibits a strong enhancement of the moist baroclinic chain, particularly in the C_A and G_E terms, as well as increased

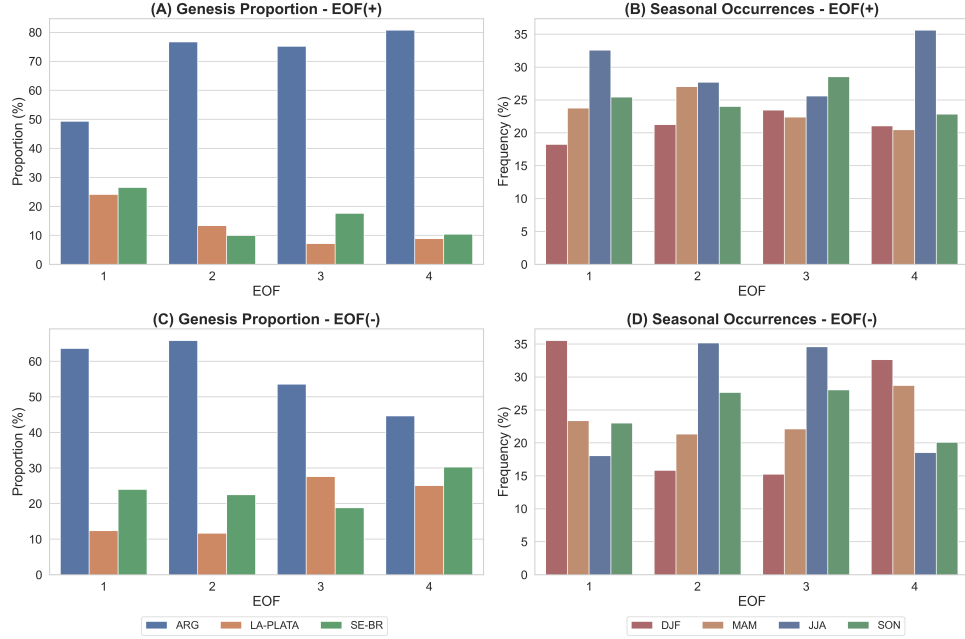


Fig. 11 Genesis proportion and seasonal occurrences of EOFs. (A) Genesis proportion for EOF(+), (B) Seasonal occurrences for EOF(+), (C) Genesis proportion for EOF(-), and (D) Seasonal occurrences for EOF(-). The colors represent different genesis regions (ARG, LA-PLATA, SE-BR) in (A) and (C), while in (B) and (D), the colors correspond to seasonal distributions (DJF, MAM, JJA, SON).

560 barotropic conversion, with both C_A and C_K contributing comparably to the K_E bud-
 561 get. However, imports of K_E are below average. Cluster 2 shows modest increases
 562 across all baroclinic and barotropic terms, with the highest K_E imports among all clus-
 563 ters. Cluster 3 displays similar proportions to Cluster 1 for C_A , C_E , and C_K , though
 564 with slightly lower values. However, it presents the highest G_E among all clusters,
 565 and unlike Cluster 1, it exhibits positive but below-average K_E imports. Cluster 4 fea-
 566 tures the weakest energy conversions overall, despite showing nearly doubled values
 567 for baroclinic and barotropic terms relative to the full-sample average, while still pre-
 568 senting below-average K_E imports. Across all clusters, the residual term is not strictly
 569 proportional to the K_E budget: Cluster 1, for instance, shows the highest RK_E despite
 570 having a lower K_E budget than Clusters 2 and 3. This suggests that, although dissipa-
 571 tion likely dominates the residual magnitude, contributions from subgrid processes
 572 and numerical errors cannot be ruled out.

573 Figure 13 displays the track density for all clusters. For all clusters, the track
 574 density maxima extend from a region near the southeastern South American coast,
 575 between $30^\circ S$ and $50^\circ S$, propagating southeastward toward the Antarctic region. Clus-
 576 ter 2 and 3 present tracks more concentrated near the continent, related to their lower
 577 mean duration (Figure S2). In contrast, Cluster 1 presents a track maxima spread

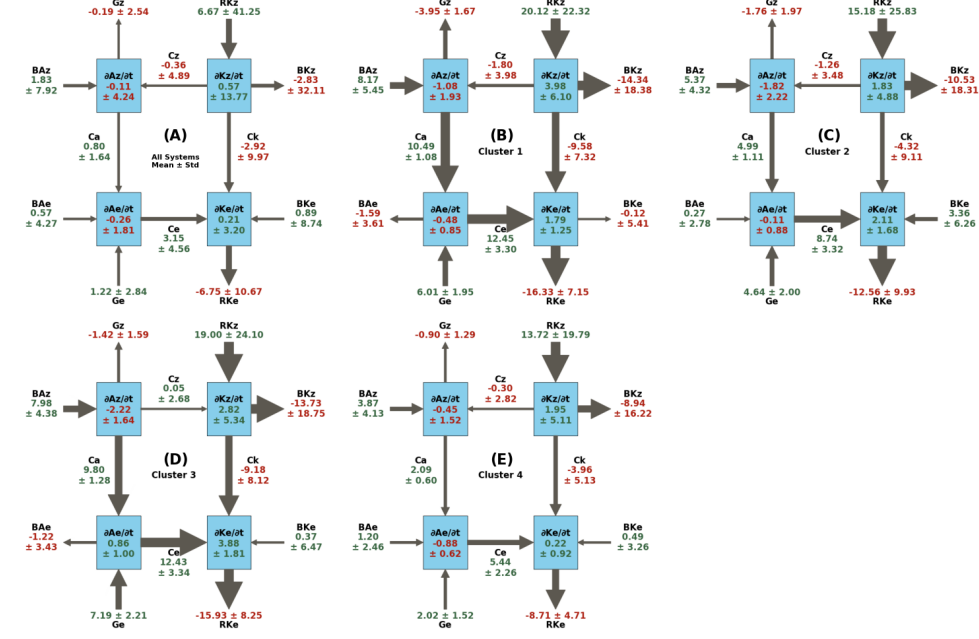


Fig. 12 (A) Mean values and standard deviations of the limited-area Lorenz Energy Cycle (LEC) terms for all analyzed systems. Panels (B–F) illustrate the reconstructed LEC for the five clusters identified among the most intense cyclones in the dataset, defined as systems with maximum central relative vorticity at 850 hPa exceeding the 90th percentile.

from near $60^{\circ}E$ to near $10^{\circ}E$. Meanwhile, Cluster 4 presents a maxima near the continent and other near Antarctica. While the track density maxima near LA-PLATA and SE-BR are associated with the incipient and intensification phases of these systems, the maxima near Antarctica correspond to their decay phase (de Souza et al., 2024). The relatively small displacement of these systems indicate that they might be related to explosive cyclogenesis and in fact, among explosive cyclogenesis in South America, evidence suggests a great contribution from LA-PLATA (Andrade et al., 2024, 2025), however, further investigation is needed to confirm this.

Clusters 1 and 2 are more frequent during JJA, while clusters 3 is more frequent during SON and Cluster 4 presents a more uniform distribution. For all clusters, the percentage of systems with genesis in LA-PLATA, in comparison with all systems in the dataset (18.9%), indicates this region as related to the development of intense systems, as previously noted by Gramscianinov et al. (2019). Also, the observed seasonality aligns with the expected behavior for LA-PLATA region (Crespo et al., 2021). The low frequency for SE-BR is also expected, as these systems are generally weaker (Gramscianinov et al., 2019; de Souza et al., 2024). Although subtropical cyclones are most frequent at SE-BR and during DJF (Evans and Braun, 2012; Gozzo et al., 2014), the low prevalence of these systems in our dataset prevent them for skewing the results.

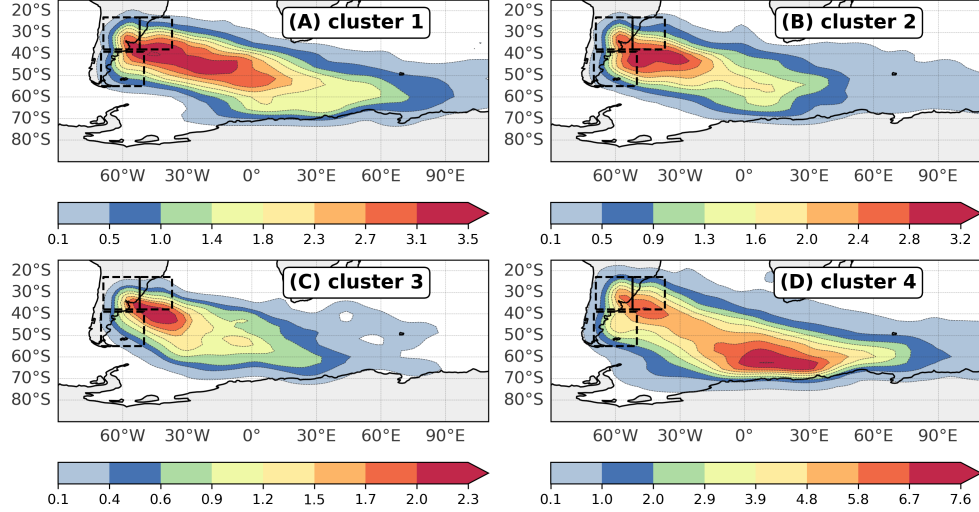


Fig. 13 Cyclone track density for the five clusters (A–E) identified among the most intense cyclones in the dataset. These systems are defined as those with maximum central relative vorticity at 850 hPa exceeding the 90th percentile. The dashed rectangles mark the genesis regions shown in Figure 1.

Clusters 1 and 2 are more frequent during JJA, while Cluster 3 peaks in SON and Cluster 4 shows no strong seasonality. In all clusters, the proportion of cyclones originating in LA-PLATA exceeds its baseline occurrence in the full dataset (18.9%), reinforcing the region’s role in the development of intense systems, as noted by Gramscianinov et al. (2019). The seasonal distributions are also consistent with prior findings for the LA-PLATA region (Crespo et al., 2021). The low frequency of cyclones forming in SE-BR is expected, as these tend to be weaker (Gramscianinov et al., 2019; de Souza et al., 2024). Although subtropical cyclones are most frequent over SE-BR during DJF (Evans and Braun, 2012; Gozzo et al., 2014), their limited presence in this intense-cyclone subset prevents them from significantly influencing the results.

4 Discussion

4.1 Key Features

The LEC diagrams (Figure 4) indicate that the mean energetic behavior is preserved across distinct life cycle phases. However, the high variability shown in Figure 3 reveals a wide range of behaviors among South Atlantic cyclones. While this section focuses on the mean energy cycle, it is important to recognize that energy budget terms serve primarily as a starting point. The energy conversions and fluxes offer more robust insight into the dynamical processes governing cyclone development. In addition to the phase-specific diagrams, a schematic of the mean Lorenz Energy Cycle for all systems is shown in Figure 15, facilitating comparison across phases and highlighting dominant pathways.

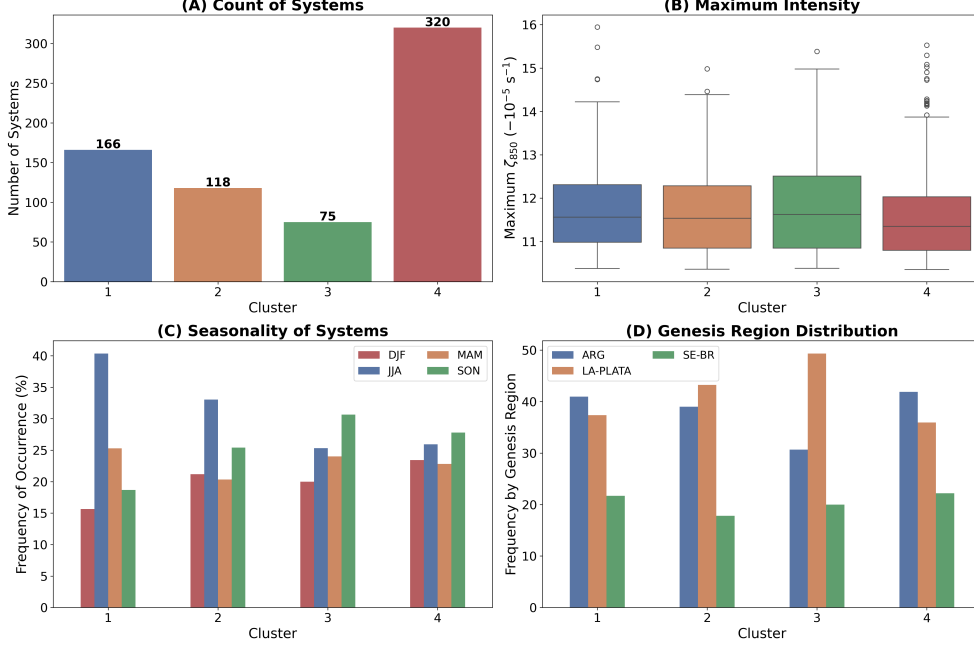


Fig. 14 Characteristics of the five clusters (A–E) identified among the most intense cyclones in the dataset. (A) Number of cyclones per cluster, (B) maximum intensity (defined as maximum central relative vorticity at 850 hPa), (C) seasonal distribution of occurrences, and (D) genesis region count. In (C), colors represent different seasons (DJF, MAM, JJA, SON), while in (D), colors correspond to genesis regions (ARG, LA-PLATA, SE-BR).

The A_Z term increases during the early phases due to persistent influxes across the boundaries ($BA_Z > 0$), rather than local generation (G_Z). As baroclinic conversions intensify, the A_Z budget becomes negative during the intensification and mature phases, before returning to positive in the decay phase. This evolution suggests that A_Z variations are not driven by latitudinal diabatic heating contrasts. A similar pattern was reported by Dias Pinto and Rocha (2011), although their methodology excluded the incipient phase due to the use of sea-level pressure for cyclone tracking, instead of relative vorticity at 850 hPa (Sinclair, 1994; Hoskins and Hodges, 2002).

For K_Z , a general increase is observed except during the mature phase, when strong barotropic conversion ($K_Z \rightarrow K_E$) coincides with negative C_Z values. This indicates descending motion at warmer latitudes and ascending motion at colder latitudes as the cold front reaches the equatorward side of the cyclone and the warm front reaches the poleward side. Notably, BK_Z and RK_Z present high magnitudes: the former suggests export of zonal kinetic energy (e.g., jet stream outflow), while the latter aggregates dissipation, boundary pressure work ($B\Phi_Z$), subgrid transfers, and numerical errors.

As the Semi-Lagrangian framework does not account for changes in the background energetics along a moving domain, part of the apparent time evolution in A_Z and K_Z may simply reflect the cyclone’s poleward drift (de Souza et al., 2024).

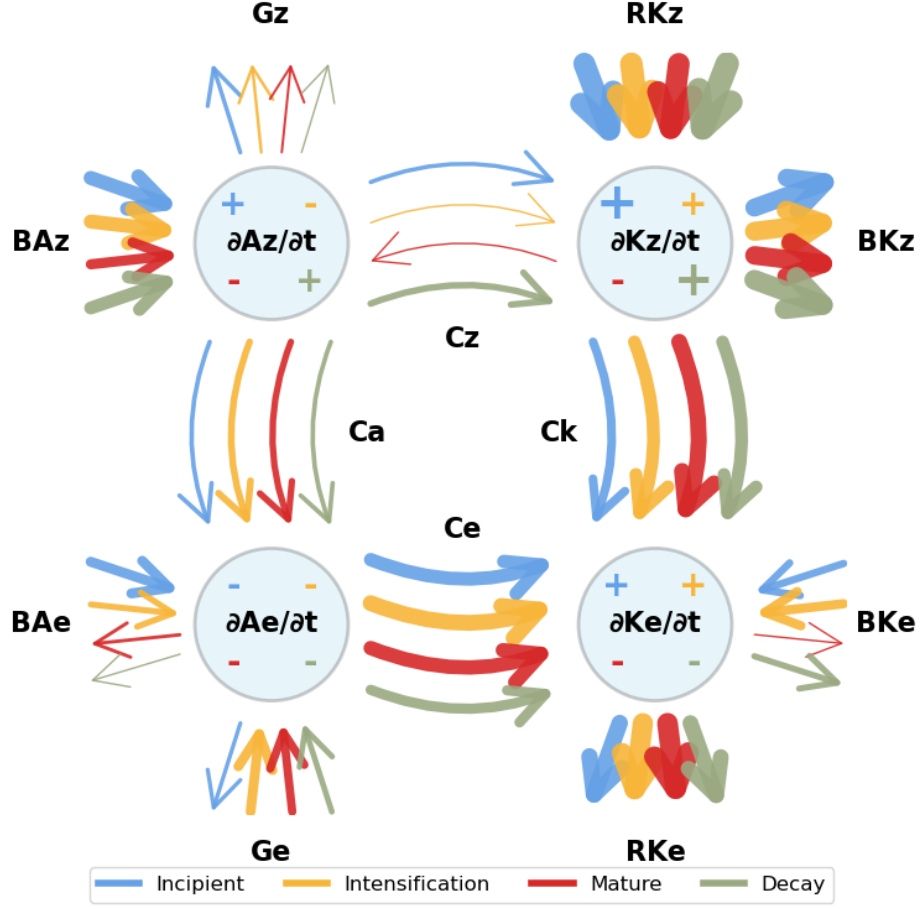


Fig. 15 Schematic representation of the mean Lorenz Energy Cycle (LEC) for all analyzed cyclones in the South Atlantic, combining information from all life cycle phases. Arrows represent energy fluxes between reservoirs, with colors indicating the life cycle phases. The arrow thicknesses and symbol sizes for the balance terms ($\partial/\partial t$) are proportional to the absolute magnitude of each term, as presented in Figure 4.

Such drift carries the system into latitudes of larger background APE, implying an increase in A_Z (Novak and Tailleux, 2018; Liu et al., 2024). Because the zonally integrated K_Z reaches its climatological maximum near 60° S (Novak and Tailleux, 2018; Liu et al., 2024), K_Z should decrease for storms that originate over ARG and migrate poleward, but increase for those formed in SE-BR or LA-PLATA. In practice, however, both reservoirs evolve irregularly and non-monotonically, indicating that intrinsic cyclone dynamics, rather than passive domain advection, control the local energetics, corroborating Federer et al. (2025).

The A_E budget is negative throughout the life cycle, with minimal values during the incipient and intensification phases. This reflects a highly active and efficient baroclinic chain. Energy is transferred from A_Z via C_A , and from A_E to K_E via C_E , driven by meridional heat transport and vertical motions in frontal zones. During intensification, G_E becomes positive, associated with convective heating along the cold front (e.g., Govekar et al., 2011). Simultaneously, radiative heating in the warm sector due to long-wave absorption from mid- to high-level clouds (Lau and Crane, 1997; Keshtgar et al., 2023), combined with latent heat release from intense precipitation during this phase (McErlich et al., 2023), enhances G_E . As the system matures and convection weakens, BA_E reverses (export), and the A_E budget sharply decreases. During decay, with disorganized frontal structures and weak diabatic forcing, A_E returns to near-zero budget values.

The K_E reservoir increases during incipient and intensification phases, as baroclinic, barotropic, and boundary fluxes supply energy. In the mature phase, barotropic conversion peaks, but weakening of baroclinic forcing and reversal of boundary fluxes, along with increased RK_E , lead to a net energy loss. During the decay phase, diminishing energy inputs and rising exports further reduce K_E . Although RK_E includes numerical errors and the $B\Phi E$ term, the trend suggests dominant dissipative processes, in line with Smith (1980).

Both $B\Phi_Z$ and $B\Phi_E$ were directly computed and yielded large values (Table 1, Figure 3d). These terms, representing pressure work by zonal and meridional winds at the domain boundaries, are highly sensitive to small errors in the geopotential field (Brennan and Vincent, 1980). Despite quality control in ERA5, some inconsistencies may persist, and since the LECTK tool does not apply preprocessing filters, such errors likely propagate into the diagnostics. Future work should examine the physical interpretation of $B\Phi$ terms and the causes of their anomalous magnitudes, as they are seldom reported in literature.

4.2 Cyclone Groups

Substantial variability in the dataset, as revealed by the EOF analysis, is largely captured by EOF1(+) and EOF1(-), which together represent nearly 40% of all systems. EOF1(+) is linked to stronger cyclones, while EOF1(-) corresponds to weaker ones (Supplementary Figure S1b), indicating a bi-modal structure in cyclone intensity. This suggests that "day-to-day" systems tend to follow distinct energetic regimes. Traditional cyclone climatologies over the South Atlantic tend to group all cyclones together (Sinclair, 1994; Hoskins and Hodges, 2005; Reboita et al., 2010; Gramscianinov et al., 2019, e.g.). In contrast, the results presented here suggest that these systems exhibit distinct behaviors and may therefore be categorized into separate groups.

These intensity differences manifest in their energy cycles and physical characteristics. Figure 16 presents schematic LECs for the four leading EOF(+) groups. EOF1(+) displays a consistent enhancement across all energy pathways, while EOF1(-) shows a reduction. These differences extend to cyclone mobility: EOF1(+) systems follow the South Atlantic storm track (Hoskins and Hodges, 2005; Gramscianinov et al., 2019), whereas EOF1(-) systems remain more confined near the South American

coast (Figure 10a), particularly within the ARG and SE-BR regions (Figure 11d), and exhibit lower translational speeds (Figure S1).

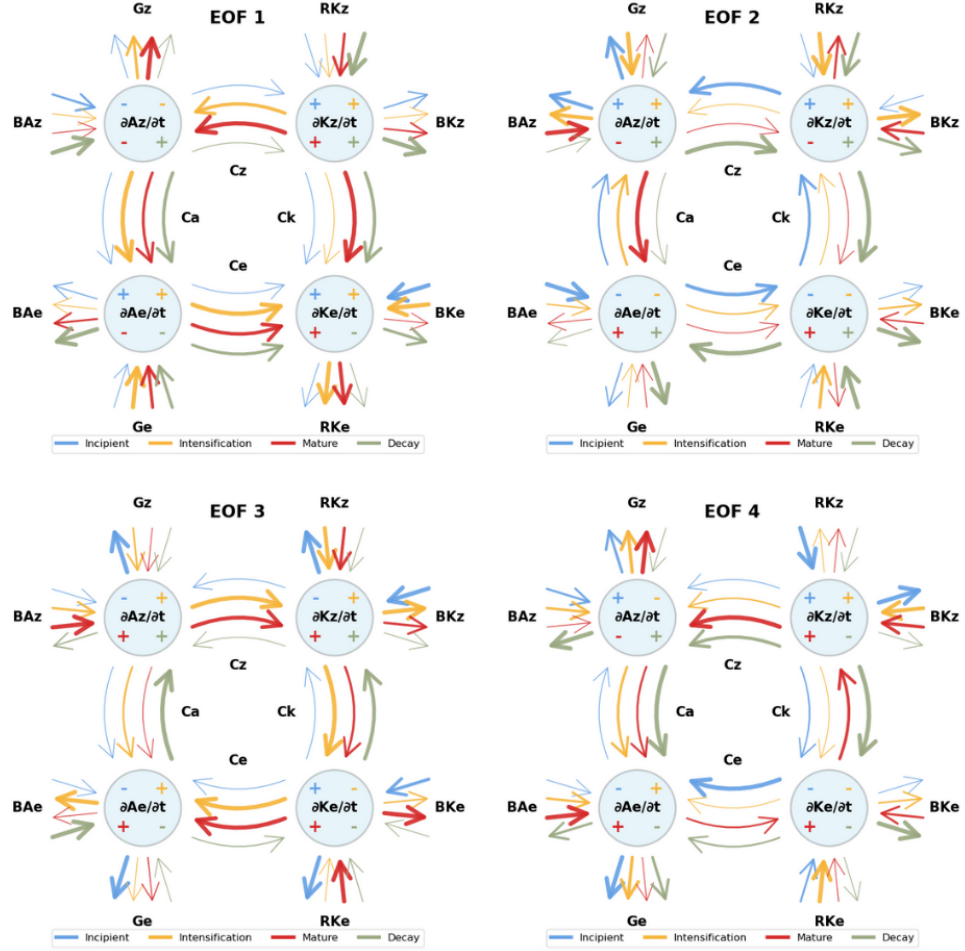


Fig. 16 Schematic representation of the mean Lorenz Energy Cycle (LEC) for cyclones associated with the four leading positive Empirical Orthogonal Functions (EOF1(+) to EOF4(+)). Arrows represent energy fluxes between reservoirs, with colors indicating life cycle phases. The thickness of each arrow and the size of the balance terms ($\partial/\partial t$) symbols are proportional to the absolute magnitude of each term.

EOF2–EOF4 describe less frequent cyclone types. EOF2(+), EOF3(–), and EOF4(–) are associated with relatively stronger systems, while their counterparts correspond to weaker ones (Figure S1b). EOF2(+) is notable for lacking enhancements in baroclinic/barotropic conversions or K_E imports during early phases. EOF3(–) and EOF4(–), in contrast, display a pronounced intensification of the $G_E \rightarrow A_E \rightarrow K_E$

chain, especially during the incipient and intensification phases. These patterns indicate that despite a shared dominant energy structure, South Atlantic cyclones express diverse configurations in their development. This variability is further reflected in differences in genesis region and seasonality (Figure 11), with EOF1(+) and EOF3(-) dominating among the most intense systems (Supplementary Figure S3).

For intense cyclones (above the 90th percentile in central vorticity), genesis is most frequent in LA-PLATA and during JJA—consistent with earlier studies identifying this region as favorable for strong development (Reboita et al., 2010; Gramscianinov et al., 2019; Crespo et al., 2021). These systems are primarily linked to moist baroclinic instability (Figure 12), particularly under the influence of a strong upper-level jet in austral winter. Meanwhile, SE-BR systems are less frequent, especially during DJF, when baroclinicity in that region is weaker (Gramscianinov et al., 2019; Crespo et al., 2021).

Among the four LEC-based clusters, Cluster 4 contains the largest number of systems but the lowest maximum central vorticity, making it the weakest group. Importantly, all clusters show enhanced LEC terms relative to the overall mean, reinforcing the connection between stronger energy fluxes and cyclone intensity. These findings support the robustness of the Semi-Lagrangian framework and highlight the existence of distinct energetic regimes. Even within the subset of intense cyclones, considerable diversity in energy cycle structures persists, indicating that multiple pathways can lead to strong cyclogenesis in the South Atlantic.

4.3 Mechanisms of Energy Transfer

Throughout this study, barotropic conversions (C_K) emerged as a key mechanism for cyclone development in the South American region. While extratropical cyclones are traditionally associated with baroclinic instability (Bjerknes and Solberg, 1922; Charney and Eliassen, 1964; Hoskins and Valdes, 1990), our results show that moist baroclinic processes dominate during the intensification phase, whereas barotropic conversions peak during the mature stage (Figure 4). Notably, C_K magnitudes are nearly three times larger than those of C_A , suggesting a stronger contribution from zonal kinetic energy to eddy development than from meridional temperature gradients.

Despite LEC-based studies dating back decades, few have examined South Atlantic cyclones, limiting direct comparisons. Case studies on tropical systems emphasize the $G_E \rightarrow A_E \rightarrow K_E$ chain and barotropic conversions (Brennan and Vincent, 1980; Veiga et al., 2008), while subtropical systems show mixed roles for both baroclinic and barotropic conversions (Michaelides, 1987; Dias Pinto et al., 2013; Pezza et al., 2014; Cavicchia et al., 2018). For extratropical systems, energy pathways vary: some are baroclinically dominated (Dias Pinto and Rocha, 2011; Black and Pezza, 2013), others barotropically (Michaelides, 1992; Dias Pinto and Rocha, 2011), and some combine both with varying degrees of K_E import (Wahab et al., 2002; Bulic, 2006; Pezza et al., 2010). Thus, although the relevance of barotropic instability in extratropical cyclones is not novel, this work provides the first large-sample LEC analysis for the South Atlantic, offering a consolidated view of this behavior. These findings are consistent with recent studies that link storm track intensification in the Southern Hemisphere to enhanced barotropic growth (Chemke et al., 2022), associate storm growth time with

738 barotropic conversion (Hadas and Kaspi, 2025), and identify barotropic conversions
739 from K_Z to K_E within storm track regions (Liu et al., 2024).

740 It is also important to emphasize that, while previous studies investigated the LEC
741 using an Eulerian framework, this study employed a Semi-Lagrangian framework. This
742 approach has the advantage of isolating the energetics strictly related to the target
743 system. However, the extent to which this methodology differs from the Eulerian
744 framework in representing the magnitude and direction of energy fluxes has not been
745 extensively assessed, apart from one study by Michaelides et al. (1999). Also, the
746 extent to which our findings generalize to other regions remains uncertain. Given the
747 stronger jets and meridional wind gradients in the Southern Hemisphere (e.g., Swart
748 et al., 2019; Jain et al., 2023; Savita et al., 2023), barotropic conversions may be more
749 pronounced in the South Atlantic than in the North Atlantic—a hypothesis requiring
750 further study.

751 Another distinction is found in the decay phase. While most previous studies report
752 $K_E \rightarrow K_Z$ conversions during cyclone decay (e.g., Dias Pinto and Rocha, 2011; Veiga
753 et al., 2008; Pezza et al., 2014), this pattern was not observed here. In our analysis,
754 the decay phase, the longest for these systems (de Souza et al., 2024), is averaged over
755 multiple timesteps and features C_K values that gradually shift from strongly negative
756 in the mature phase to near neutral at the end of the lifecycle (Figures 4C and S4). This
757 suggests that barotropic conversion continues to sustain the system during decay, until
758 dissipation dominates. Prior use of large Eulerian domains may have underestimated
759 C_K , as seen in Black and Pezza (2013), where C_K remains positive across all phases.

760 Some limitations of our approach must be acknowledged. Although the Semi-
761 Lagrangian framework follows the cyclone’s trajectory, it does not account for regional
762 variations in background APE and kinetic energy. This may influence A_Z , K_Z , and
763 their boundary terms as the system moves through varying energy environments.
764 Furthermore, the LEC formulation relies on a global reference state for APE. In
765 contrast, the local APE framework proposed by Novak and Tailleux (2018) defines
766 APE relative to each air parcel’s individual reference state. While this approach can
767 yield additional insights—such as the potential for cyclones to locally generate APE
768 (Federer et al., 2024), the overall global energy fluxes remain consistent between the
769 global and local formulations (Liu et al., 2024). Moreover, the modest BA_Z values
770 observed here (Figure 4) may be partially explained by APE transport from the polar
771 upper troposphere, as shown for the North Atlantic storm tracks by Federer et al.
772 (2025).

773 5 Summary and Conclusions

774 In this study, we examined the Lorenz Energy Cycle (LEC) for 7,531 cyclonic systems
775 originating in the Southwestern Atlantic, presenting what is, to the best of our knowl-
776 edge, the first comprehensive climatology of cyclones’ energy cycles in this region. A
777 notable exception is the work by Black and Pezza (2013), which focused solely on
778 explosive cyclones and used large fixed domains, contrasting with the Semi-Lagrangian
779 approach adopted in this study. While studies such as Smith (1980) provide valuable
780 reviews of the energetics of extratropical cyclones, focusing on broad averages and

generalized mechanisms, and case studies have explored the dynamics of specific systems (Pezza et al., 2014; Dias Pinto and Rocha, 2011; Cavicchia et al., 2018, e.g.), our study adopts a climatological approach. Specifically, we track the energy cycles of individual cyclones across distinct life cycle phases, offering a more detailed investigation of the unique physical mechanisms that drive energy conversions in this region. Furthermore, the use of the Cyclophaser program to dissect the life cycles of cyclones has enabled a novel investigation of the energy cycle across different developmental stages, providing deeper insights into the variability and dynamism of these systems.

The results presented here demonstrate that, for most cyclonic systems in the South Atlantic, a clear pattern of energy flow is evident. This pattern is characterized by both barotropic and baroclinic conversions providing energy for eddy development and is preserved throughout the cyclone life cycle phases, despite variations in magnitude. Barotropic conversions tend to be 2 to 3 times larger in magnitude than baroclinic conversions, with the former peaking during the mature phase and the latter during the intensification phase. The generation of eddy potential energy and the imports of eddy kinetic energy play secondary roles. The former peaks during the intensification phase and remains positive through the mature and decay phases, while the latter occurs primarily during the incipient (cyclogenesis) and intensification phases.

Despite the high variability among the systems, the EOF analysis indicates that, in most cases, the main behavior is preserved. This variability is instead expressed as a strengthening and/or weakening of specific energy pathways, indicating that cyclonic development in the South Atlantic region can be attributed to distinct dynamical processes, as supported by the literature. Consequently, it is possible to hypothesize that these systems can be grouped into distinct types based on their characteristics and energy cycles. This heterogeneity is also evident among the most intense systems. For these systems, distinct groups exhibit varying relative contributions of energy from barotropic and baroclinic chains, as well as differences in eddy generation of APE and imports of eddy kinetic energy. Although most of these intense systems originate in the LA-PLATA region, the variability in the relative proportions of genesis regions among the different clusters is reflected in their energy cycles and mean characteristics.

The goal of this study was to investigate the energy cycle of cyclones in the South Atlantic region using a Semi-Lagrangian approach. As a pioneering study of this kind, several questions have emerged throughout its development. For instance, previous studies for this region have assessed the distinct synoptic and dynamical conditions related to cyclogenesis in the three primary genesis regions, as well as the seasonal variability in their development (Gramscianinov et al., 2019; Crespo et al., 2021). A distinction in the energy cycles among these genesis regions, along with their seasonal variability, would therefore be valuable. Additionally, given the prominence of barotropic conversions as an energy source for cyclone development, the question arises as to whether barotropic instability is truly occurring near the cyclone center. de Souza (2024) proposed a framework for classifying cyclones into distinct groups based on their energy cycles. In an upcoming study, this method will be applied to address these questions and further investigate these topics.

825 Appendix

826 Mathematical expressions used for the calculation of the Lorenz Energy Cycle (LEC),
827 adopting the notation from Michaelides (1987).

828 Firstly, we define the zonal mean of a variable X , between longitudes λ_1 and λ_2 :

$$[X]_\lambda = \frac{1}{\lambda_2 - \lambda_1} \int_{\lambda_2}^{\lambda_1} X d\lambda \quad (13)$$

829 The eddy component of this variable is its deviation from the zonal mean:

$$(X)_\lambda = X - [X]_\lambda \quad (14)$$

830 The domain mean of the variable X , defined over the computational domain
831 bounded by longitudes λ_1 and λ_2 , and latitudes ϕ_1 and ϕ_2 , is given by:

$$[X]_{\lambda\phi} = \left(\frac{1}{\lambda_2 - \lambda_1} \right) \left(\frac{1}{\sin \phi_2 - \sin \phi_1} \right) \int_{\lambda_2}^{\lambda_1} X \cos \phi d\lambda d\phi \quad (15)$$

832 Similarly, we define the deviation of the zonal mean from the domain mean:

$$([X]_\lambda)_\phi = [X]_\lambda - [X]_{\lambda\phi} \quad (16)$$

833 From the definitions above, the four energy components used in the LEC
834 computation are defined as follows:

$$A_Z = \int_{p_t}^{p_b} \frac{[(T)_\lambda]^2_{\lambda\phi}}{2[\sigma]_{\lambda\phi}} dp \quad (17)$$

$$A_E = \int_{p_t}^{p_b} \frac{[(T)_\lambda^2]_{\lambda\phi}}{2[\sigma]_{\lambda\phi}} dp \quad (18)$$

$$K_Z = \int_{p_t}^{p_b} \frac{[u]_\lambda^2 + [v]_\lambda^2_{\lambda\phi}}{2g} dp \quad (19)$$

$$K_E = \int_{p_t}^{p_b} \frac{[(u)_\lambda^2 + (v)_\lambda^2]_{\lambda\phi}}{2g} dp \quad (20)$$

835 where p is the atmospheric pressure, with subscripts b and t denoting the lower
836 (base) and upper (top) pressure boundaries of the atmosphere, respectively. T repre-
837 sents temperature, g is the acceleration due to gravity, and u and v are the zonal and
838 meridional wind components, respectively. The static stability parameter σ is defined
839 as:

$$\sigma = \left[\frac{gT}{c_p} - \frac{pg}{R} \frac{\partial T}{\partial p} \right]_{\lambda\phi} \quad (21)$$

840 where c_p is the specific heat at constant pressure, and R is the ideal gas constant
841 for dry air.

842 The four conversion terms are defined as follows, integrating over the atmospheric
843 column from the base (p_b) to the top (p_t) pressures:

$$C_Z = \int_{p_t}^{p_b} -[([T]_\lambda)_\phi([\omega]_\lambda)_\phi]_{\lambda\phi} \frac{R}{gp} dp \quad (22)$$

$$C_E = \int_{p_t}^{p_b} -[(T)_\lambda(\omega)_\lambda]_{\lambda\phi} \frac{R}{gp} dp \quad (23)$$

$$C_A = \int_{p_t}^{p_b} -\left(\frac{1}{2a\sigma} \left[(v)_\lambda(T)_\lambda \frac{\partial([T]_\lambda)_\phi}{\partial\phi} \right]_{\lambda\phi} + \frac{1}{\sigma} \left[(\omega)_\lambda(T)_\lambda \frac{\partial([T]_\lambda)_\phi}{\partial p} \right]_{\lambda\phi} \right) dp \quad (24)$$

$$C_K = \int_{p_t}^{p_b} \frac{1}{g} \left(\left[\frac{\cos\phi}{a} (u)_\lambda(v)_\lambda \frac{\partial}{\partial\phi} \left(\frac{[u]_\lambda}{\cos\phi} \right) \right]_{\lambda\phi} + \left[\frac{(v)_\lambda^2}{a} \frac{\partial[v]_\lambda}{\partial\phi} \right]_{\lambda\phi} + \left[\frac{\tan\phi}{a} (u)_\lambda^2 [v]_\lambda \right]_{\lambda\phi} + \left[(\omega)_\lambda(u)_\lambda \frac{\partial[u]_\lambda}{\partial p} \right]_{\lambda\phi} + \left[(\omega)_\lambda(v)_\lambda \frac{\partial[v]_\lambda}{\partial p} \right]_{\lambda\phi} \right) dp \quad (25)$$

where a is the Earth's radius and ω is the vertical velocity in isobaric coordinates.
The APE generation and K dissipation terms are defined as:

$$G_Z = \int_{p_t}^{p_b} \frac{[(q)_\lambda)_\phi([T]_\lambda)_\phi]_{\lambda\phi}}{c_p[\sigma]_{\lambda\phi}} dp \quad (26)$$

$$G_E = \int_{p_t}^{p_b} \frac{[(q)_\lambda(T)_\lambda]_{\lambda\phi}}{c_p[\sigma]_{\lambda\phi}} dp \quad (27)$$

$$D_Z = - \int_{p_t}^{p_b} \frac{1}{g} [[u]_\lambda[F_\lambda]_\lambda + [v]_\lambda[F_\phi]_\lambda]_{\lambda\phi} dp \quad (28)$$

$$D_E = - \int_{p_t}^{p_b} \frac{1}{g} [(u)_\lambda(F_\lambda)_\lambda + (v)_\lambda(F_\phi)_\lambda]_{\lambda\phi} dp \quad (29)$$

Here, F_λ and F_ϕ represent the zonal and meridional frictional components, respectively, and q is the diabatic heating term, computed as a residual from the thermodynamic equation:

$$\frac{q}{c_p} = \frac{\partial T}{\partial t} - \vec{V}_H \cdot \vec{\nabla}_p T - S_p \omega \quad (30)$$

where $-\vec{V}_H \cdot \vec{\nabla}_p T$ represents the horizontal advection of temperature and S_p approximates the static stability, given by:

$$S_p \equiv -\frac{T}{\theta} \frac{\partial \theta}{\partial p} \quad (31)$$

where θ is the potential temperature.

The boundary terms are given by:

$$\begin{aligned}
\text{BAZ} = & c_1 \int_{p_1}^{p_2} \int_{\varphi_1}^{\varphi_2} \frac{1}{2[\sigma]_{\lambda\varphi}} \left(2 ([T]_{\lambda})_{\varphi} (T)_{\lambda} u + ([T]_{\lambda\varphi})_{\varphi}^2 u \right)_{\lambda_1}^{\lambda_2} \\
& \times d\varphi dp + c_2 \int_{p_1}^{p_2} \frac{1}{2[\sigma]_{\lambda\varphi}} \left(2 [(v)_{\lambda}(T)_{\lambda}]_{\lambda} ([T]_{\lambda})_{\varphi} \cos \varphi + ([T]_{\lambda})_{\varphi}^2 [v]_{\lambda} \cos \varphi \right)_{\varphi_1}^{\varphi_2} dp \\
& - \frac{1}{2[\sigma]_{\lambda\varphi}} \left([2(\omega)_{\lambda}(T)_{\lambda}]_{\lambda} ([T]_{\lambda})_{\varphi} + [[\omega]_{\lambda} ([T]_{\lambda})_{\varphi}^2]_{\lambda\varphi} \right)_{p_1}^{p_2} \quad (32)
\end{aligned}$$

$$\begin{aligned}
\text{BAE} = & c_1 \int_{p_1}^{p_2} \int_{\varphi_1}^{\varphi_2} \frac{1}{2[\sigma]_{\lambda\varphi}} [u(T)_{\lambda}^2]_{\lambda_1}^{\lambda_2} d\varphi dp \\
& + c_2 \int_{p_1}^{p_2} \frac{1}{2[\sigma]_{\lambda\varphi}} \left([(T)_{\lambda}^2 v]_{\lambda} \cos \varphi \right)_{\varphi_1}^{\varphi_2} dp \\
& - \left(\frac{[\omega(T)_{\lambda}^2]_{\lambda\varphi}}{2[\sigma]_{\lambda\varphi}} \right)_{p_1}^{p_2} \quad (33)
\end{aligned}$$

$$\begin{aligned}
\text{BKZ} = & c_1 \int_{p_1}^{p_2} \int_{\varphi_1}^{\varphi_2} \frac{1}{2g} \left(u [u^2 + v^2 - (u)_{\lambda}^2 - (v)_{\lambda}^2] \right)_{\lambda_1}^{\lambda_2} \\
& \times d\varphi dp + c_2 \int_{p_1}^{p_2} \frac{1}{2g} \left([v \cos \varphi [u^2 + v^2 - (u)_{\lambda}^2 - (v)_{\lambda}^2]]_{\varphi_1}^{\varphi_2} \right) dp \\
& - \left(\frac{1}{2g} [\omega [u^2 + v^2 - (u)_{\lambda}^2 - (v)_{\lambda}^2]]_{\lambda\varphi} \right)_{p_1}^{p_2} \quad (34)
\end{aligned}$$

$$\begin{aligned}
\text{BKE} = & c_1 \int_{p_1}^{p_2} \int_{\varphi_1}^{\varphi_2} \frac{1}{2g} \left(u [(u)_{\lambda}^2 + (v)_{\lambda}^2] \right)_{\lambda_1}^{\lambda_2} d\varphi dp \\
& + c_2 \int_{p_1}^{p_2} \frac{1}{2g} \left([v \cos \varphi [(u)_{\lambda}^2 + (v)_{\lambda}^2]]_{\lambda} \right)_{\varphi_1}^{\varphi_2} dp \\
& - \left(\frac{1}{2g} [\omega [(u)_{\lambda}^2 + (v)_{\lambda}^2]]_{\lambda\varphi} \right)_{p_1}^{p_2} \quad (35)
\end{aligned}$$

853 where $c_1 = -[a(\lambda_2 - \lambda_1)(\sin \varphi_2 - \sin \varphi_1)]^{-1}$, $c_2 = -[a \ x(\sin \varphi_2 - \sin \varphi_1)]^{-1}$.
854 Lastly, the terms $B\Phi Z$ and $B\Phi E$ are given by:

$$\begin{aligned}
\text{B}\Phi\text{Z} = & c_1 \int_{p_1}^{p_2} \int_{\varphi_1}^{\varphi_2} \frac{1}{g} \left([v]_{\lambda} ([\Phi]_{\lambda})_{\varphi} \right)_{\lambda_1}^{\lambda_2} d\varphi dp \\
& + c_2 \int_{p_1}^{p_2} \frac{1}{g} \left(\cos \varphi [v]_{\lambda} ([\Phi]_{\lambda})_{\varphi} \right)_{\varphi_1}^{\varphi_2} dp \\
& - \frac{1}{g} \left([([\omega]_{\lambda})_{\varphi} ([\Phi]_{\lambda})_{\varphi}]_{\lambda\varphi} \right)_{p_1}^{p_2} \\
\text{B}\Phi\text{E} = & c_1 \int_{p_1}^{p_2} \int_{\varphi_1}^{\varphi_2} \frac{1}{g} ((u)_{\lambda}(\Phi)_{\lambda})_{\lambda_1}^{\lambda_2} d\varphi dp \quad (36)
\end{aligned}$$

$$\begin{aligned}
& + c_2 \int_{p_1}^{p_2} \frac{1}{g} \left([(\nu)_\lambda(\Phi)_{\lambda_\lambda}]_\lambda \cos \varphi \right)_{\varphi_1}^{\varphi_2} dp \\
& - \frac{1}{g} \left([(\omega)_\lambda(\Phi)_{\lambda_\lambda}]_{\lambda_\varphi} \right)_{p_1}^{p_2}
\end{aligned} \tag{37}$$

Declarations

Funding

This study was partly financed by the Coordenação de Aperfeiçoamento de Pessoal de Nível Superior – Brasil (CAPES) under Finance Code 001.

Competing interests

The authors have no relevant financial or non-financial interests to disclose.

Data Availability

The cyclone tracks used in this study were obtained from the *Atlantic Extratropical Cyclone Tracks Database*, available at <https://doi.org/10.17632/kwcvfr52hp.4>. All datasets, including the computed Lorenz Energy Cycle results for each cyclone, along with the scripts used to generate the figures and analyses presented in this study, are publicly available at the following GitHub repository: https://github.com/daniloceano/energetic_patterns_cyclones_south_atlantic. The source code of the **Cyclophaser** package, used for detecting cyclone life cycle phases, is available on PyPI at <https://pypi.org/project/cyclophaser/>. The **LorenzCycleToolkit** package, used for computing the Lorenz Energy Cycle components, is also available on PyPI at <https://pypi.org/project/LorenzCycleToolkit/>.

Author contributions

Conceptualization: Danilo Couto de Souza, Pedro Leite da Silva Dias, Ricardo de Camargo, Carolina Barnez Gramscianinov; Methodology: Danilo Couto de Souza, Pedro Leite da Silva Dias, Ricardo de Camargo; Formal analysis and investigation: Danilo Couto de Souza, Pedro Leite da Silva Dias; Writing - original draft preparation: Danilo Couto de Souza; Writing - review and editing: Danilo Couto de Souza, Pedro Leite da Silva Dias, Ricardo de Camargo, Carolina Barnez Gramscianinov; Funding acquisition: Pedro Leite da Silva Dias, Ricardo de Camargo; Resources: Pedro Leite da Silva Dias, Ricardo de Camargo; Supervision: Pedro Leite da Silva Dias, Ricardo de Camargo.

References

- Andrade, H.N., A.B. Nunes, M.S. Teixeira, M.F.L. de Quadro, V.D. de Avila, F.S.C. de Oliveira, and R.d.C.M. Alves. 2025. Composite analysis of explosive cyclones in the southern atlantic ocean. *International Journal of Climatology* 45(4): e8737 .

- 886 Andrade, H.N., M.F.L.D. Quadro, A.B. Nunes, F.S.D. Oliveira, V.D.D. Avila, M.S.
887 Teixeira, and R.D.C.M. Alves. 2024. Explosive cyclones occurred between 2010 and
888 2020 in the south atlantic under the perspective of two detection schemes. *Anais*
889 *da Academia Brasileira de Ciências* 96(suppl 1): e20231051 .
- 890 Bengfort, B. and R. Bilbro. 2019. Yellowbrick: Visualizing the scikit-learn model
891 selection process. *Journal of Open Source Software* 4(35): 1075 .
- 892 Bjerknes, J. and H. Solberg. 1922. *Life cycle of cyclones and the polar front theory of*
893 *atmospheric circulation*. Grondahl.
- 894 Black, M.T. and A.B. Pezza. 2013. A universal, broad-environment energy conversion
895 signature of explosive cyclones. *Geophysical Research Letters* 40(2): 452–457 .
- 896 Brennan, F.E. and D.G. Vincent. 1980. Zonal and eddy components of the synoptic-
897 scale energy budget during intensification of hurricane carmen (1974). *Monthly*
898 *Weather Review* 108(7): 954–965. [https://doi.org/10.1175/1520-0493\(1980\)](https://doi.org/10.1175/1520-0493(1980)108<0954:ZAECOT>2.0.CO;2)
899 108<0954:ZAECOT>2.0.CO;2 .
- 900 Bulic, I. 2006. Limited area energy budget during a life cycle of genoa cyclone
901 (18-21 november 1999). *NUOVO CIMENTO-SOCIETA ITALIANA DI FISICA*
902 *SEZIONE C* 29(2): 167 .
- 903 Cardoso, A.A., R.P. da Rocha, and N.M. Crespo. 2022. Synoptic climatology of
904 subtropical cyclone impacts on near-surface winds over the south atlantic basin.
905 *Earth and Space Science* 9(11): e2022EA002482 .
- 906 Cavicchia, L., A. Dowdy, and K. Walsh. 2018. Energetics and dynamics of sub-
907 tropical australian east coast cyclones: Two contrasting cases. *Monthly Weather*
908 *Review* 146(5): 1511–1525 .
- 909 Charney, J.G. and A. Eliassen. 1964. On the growth of the hurricane depression.
910 *Journal of the Atmospheric Sciences* 21(1): 68–75 .
- 911 Chemke, R., Y. Ming, and J. Yuval. 2022. The intensification of winter mid-latitude
912 storm tracks in the southern hemisphere. *Nature climate change* 12(6): 553–557 .
- 913 Crespo, N.M., R.P. da Rocha, M. Sprenger, and H. Wernli. 2021. A potential vorticity
914 perspective on cyclogenesis over centre-eastern south america. *International Journal*
915 *of Climatology* 41(1): 663–678 .
- 916 da Silva, M.B.L., D.C. de Souza, F.T.C. Barreto, R. Tecchio, R. de Freitas
917 Pimentel dos Anjos, C.B. Gramscianinov, and R. De Camargo. 2025. Classifica-
918 tion of synoptic weather patterns associated with extreme wave events in different
919 regions of western south atlantic. *Natural Hazards*: 1–25 .

- de Souza, D. and R.R. da Silva. 2021. Ocean-land atmosphere model (olam) performance for major extreme meteorological events near the coastal region of southern brazil. *Climate Research* 84: 1–21 .
- de Souza, D.C. 2024. *Cyclones in the Southwestern Atlantic: Life Cycle and Energetics*. Doctoral thesis, Universidade de São Paulo, São Paulo, Brazil. Versão corrigida.
- de Souza, D.C., N.M. Crespo, D.V. da Silva, L.M. Harada, R.M.P. de Godoy, L.M. Domingues, R. Luiz, C.A. Bortolozo, D. Metodiev, M.R.M. de Andrade, et al. 2024. Extreme rainfall and landslides as a response to human-induced climate change: a case study at baixada santista, brazil, 2020. *Natural Hazards*: 1–26 .
- de Souza, D.C., P.L.S. da Dias, M.B.L. da Silva, and R. de Camargo. 2024. Lorenz-cycletoolkit: A comprehensive python tool for analyzing atmospheric energy cycles. *Journal of Open Source Software* 9(101): 7139 .
- de Souza, D.C., P.L.S. da Dias, C.B. Gramscianinov, and R. de Camargo. 2025. Cyclophaser: A python package for detecting extratropical cyclone life cycles. *Journal of Open Source Software* 10(108): 7363 .
- de Souza, D.C., P.L. da Silva Dias, C.B. Gramscianinov, M.B.L. da Silva, and R. de Camargo. 2024. New perspectives on south atlantic storm track through an automatic method for detecting extratropical cyclones’ lifecycle. *International Journal of Climatology* 44(10): 3568–3588 .
- de Souza, D.C., R. Ramos da Silva, P. Gomes da Silva, A.F.H. Fetter Filho, F.J. Mendez, and D. Werth. 2022. A hybrid regional climate downscaling for the southern brazil coastal region. *International Journal of Climatology* 42(13): 6753–6770 .
- de Souza, D.C., V.A. Ranieri, P.L. da Silva Dias, A.R. Flores, and R. de Camargo. 2025. Revisiting the rare transition of a south atlantic cyclone to tropical storm akar: Energy cycle and stratosphere-troposphere interaction. manuscript submitted to Climate Dynamics. Preprint available at <https://scity.org/articles/activity/10.21203/rs.3.rs-6536558/v1>.
- Dias Pinto, J.R., M.S. Reboita, and R.P. da Rocha. 2013. Synoptic and dynamical analysis of subtropical cyclone anita (2010) and its potential for tropical transition over the south atlantic ocean. *Journal of Geophysical Research: Atmospheres* 118(19): 10–870. <https://doi.org/10.1002/jgrd.50830> .
- Dias Pinto, J.R. and R.P. Rocha. 2011. The energy cycle and structural evolution of cyclones over southeastern south america in three case studies. *Journal of Geophysical Research: Atmospheres* 116(D14) .

- 956 Dutton, J.A. and D.R. Johnson. 1967. The theory of available potential energy and a
957 variational approach to atmospheric energetics. *Advances in geophysics* 12: 333–436
958 .
- 959 Evans, J.L. and A. Braun. 2012. A climatology of subtropical cyclones in the south
960 atlantic. *Journal of Climate* 25(21): 7328–7340 .
- 961 Federer, M., L. Papritz, M. Sprenger, and C.M. Grams. 2025. Synoptic perspective on
962 the conversion and maintenance of local available potential energy in extratropical
963 cyclones. *Weather and Climate Dynamics* 6(1): 211–230 .
- 964 Federer, M., L. Papritz, M. Sprenger, C.M. Grams, and M. Wenta. 2024. On the local
965 available potential energy perspective of baroclinic wave development. *Journal of
966 the Atmospheric Sciences* 81(5): 871–886 .
- 967 Fukuoka, A. 1951. A study of 10-day forecast (a synthetic report). *The Geophysical
968 Magazine* XXII: 177–218 .
- 969 Govekar, P.D., C. Jakob, M.J. Reeder, and J. Haynes. 2011. The three-dimensional dis-
970 tribution of clouds around southern hemisphere extratropical cyclones. *Geophysical
971 Research Letters* 38(21). <https://doi.org/10.1029/2011GL049091> .
- 972 Gozzo, L.F., R.P. da Rocha, M.S. Reboita, and S. Sugahara. 2014. Subtropical
973 cyclones over the southwestern south atlantic: Climatological aspects and case
974 study. *Journal of Climate* 27(22): 8543–8562 .
- 975 Gramscianinov, C., R. Campos, R. De Camargo, K. Hodges, C.G. Soares, and
976 P. da Silva Dias. 2020. Analysis of atlantic extratropical storm tracks characteristics
977 in 41 years of era5 and cfsr/cfsv2 databases. *Ocean Engineering* 216: 108–111 .
- 978 Gramscianinov, C., K. Hodges, and R.d. Camargo. 2019. The properties and genesis
979 environments of south atlantic cyclones. *Climate Dynamics* 53: 4115–4140 .
- 980 Gramscianinov, C.B., R.M. Campos, R. de Camargo, K.I. Hodges, C. Guedes Soares,
981 and P.L. da Silva Dias. 2020. Atlantic extratropical cyclone tracks in 41 years of
982 ERA5 and CFSR/CFSv2 databases. *Mendeley Data* V4. [https://doi.org/10.17632/
983 kwcvfr52hp.4](https://doi.org/10.17632/kwcvfr52hp.4) .
- 984 Gramscianinov, C.B., R. de Camargo, R.M. Campos, C. Guedes Soares, and P.L.
985 da Silva Dias. 2023. Impact of extratropical cyclone intensity and speed on the
986 extreme wave trends in the atlantic ocean. *Climate dynamics* 60(5-6): 1447–1466 .
- 987 Gutierrez, E.R., P.S. Dias, J. Veiga, R. Camayo, and A. Dos Santos. 2009. Multivariate
988 analysis of the energy cycle of the south american rainy season. *International
989 Journal of Climatology* 29(15): 2256–2269 .

- 990 Hadas, O. and Y. Kaspi. 2025. A lagrangian perspective on the growth of midlatitude
991 storms. *AGU Advances* 6(3): e2024AV001555 .
- 992 Hao, J. and T.K. Ho. 2019. Machine learning made easy: a review of scikit-learn
993 package in python programming language. *Journal of Educational and Behavioral*
994 *Statistics* 44(3): 348–361 .
- 995 Hartigan, J.A. and M.A. Wong. 1979. Algorithm as 136: A k-means clustering algo-
996 rithm. *Journal of the Royal Statistical Society. Series C (Applied Statistics)* 28(1):
997 100–108 .
- 998 Hernández-Deckers, D. and J.S. von Storch. 2010. Energetics responses to increases
999 in greenhouse gas concentration. *Journal of Climate* 23(14): 3874–3887 .
- 1000 Hersbach, H., B. Bell, P. Berrisford, S. Hirahara, A. Horányi, J. Muñoz-Sabater,
1001 J. Nicolas, C. Peubey, R. Radu, D. Schepers, et al. 2020. The era5 global reanalysis.
1002 *Quarterly Journal of the Royal Meteorological Society* 146(730): 1999–2049 .
- 1003 Hodges, K. 1995. Feature tracking on the unit sphere. *Monthly Weather*
1004 *Review* 123(12): 3458–3465 .
- 1005 Hodges, K.I. 1994. A general method for tracking analysis and its application to
1006 meteorological data. *Monthly Weather Review* 122(11): 2573–2586 .
- 1007 Hoskins, B.J. and K.I. Hodges. 2002. New perspectives on the northern hemisphere
1008 winter storm tracks. *Journal of the Atmospheric Sciences* 59(6): 1041–1061. [https://doi.org/10.1175/1520-0469\(2002\)059<1041:NPOTNH>2.0.CO;2](https://doi.org/10.1175/1520-0469(2002)059<1041:NPOTNH>2.0.CO;2) .
- 1009
- 1010 Hoskins, B.J. and K.I. Hodges. 2005. A new perspective on southern hemisphere
1011 storm tracks. *Journal of Climate* 18(20): 4108–4129 .
- 1012 Hoskins, B.J. and P.J. Valdes. 1990. On the existence of storm-tracks. *Journal of*
1013 *Atmospheric Sciences* 47(15): 1854–1864 .
- 1014 Hu, Q., Y. Tawaye, and S. Feng. 2004. Variations of the northern hemisphere
1015 atmospheric energetics: 1948–2000. *Journal of Climate* 17(10): 1975–1986 .
- 1016 Jain, D., S.A. Rao, R. Dandi, P.A. Pillai, A. Srivastava, and M. Pradhan. 2023.
1017 Monsoon mission coupled forecast system version 2.0: model description and indian
1018 monsoon simulations. *Geoscientific Model Development Discussions* 2023: 1–29 .
- 1019 Keshtgar, B., A. Voigt, C. Hoose, M. Riemer, and B. Mayer. 2023. Cloud-
1020 radiative impact on the dynamics and predictability of an idealized extratropical
1021 cyclone. *Weather and Climate Dynamics* 4(1): 115–132. <https://doi.org/10.5194/wcd-4-115-2023> .
- 1022
- 1023 Kirshbaum, D., T. Merlis, J. Gyakum, and R. McTaggart-Cowan. 2018. Sensitivity
1024 of idealized moist baroclinic waves to environmental temperature and moisture

- 1025 content. *Journal of the Atmospheric Sciences* 75(1): 337–360 .
- 1026 Lau, N.C. and M.W. Crane. 1997. Comparing satellite and surface observa-
 1027 tions of cloud patterns in synoptic-scale circulation systems. *Monthly weather*
 1028 *review* 125(12): 3172–3189. [https://doi.org/10.1175/1520-0493\(1997\)125\(3172:](https://doi.org/10.1175/1520-0493(1997)125(3172:CSASOO)2.0.CO;2)
 1029 [CSASOO\)2.0.CO;2](https://doi.org/10.1175/1520-0493(1997)125(3172:CSASOO)2.0.CO;2) .
- 1030 Leal, K.B., L.E.d.S. Robaina, T.S. Körting, J.L. Nicolodi, J.D. da Costa, and V.G.
 1031 Souza. 2023. Identification of coastal natural disasters using official databases to
 1032 provide support for the coastal management: the case of santa catarina, brazil.
 1033 *Natural Hazards*: 1–18 .
- 1034 Li, L., A.P. Ingersoll, X. Jiang, D. Feldman, and Y.L. Yung. 2007. Lorenz energy
 1035 cycle of the global atmosphere based on reanalysis datasets. *Geophysical Research*
 1036 *Letters* 34(16) .
- 1037 Liu, Z., C.L. Franzke, L. Novak, R. Tailleux, and V. Lembo. 2024. A systematic
 1038 local view of the long-term changes in the atmospheric energy cycle. *Journal of*
 1039 *Climate* 37(23): 6413–6434 .
- 1040 Lorenz, E. 1967. The nature and theory of the general circulation of the atmosphere.
 1041 *World meteorological organization* 161 .
- 1042 Lorenz, E.N. 1955. Available potential energy and the maintenance of the general
 1043 circulation. *Tellus* 7(2): 157–167 .
- 1044 Lorenz, E.N. 1956. *Empirical orthogonal functions and statistical weather predic-*
 1045 *tion*, Volume 1. Massachusetts Institute of Technology, Department of Meteorology
 1046 Cambridge.
- 1047 MacQueen, J. et al. 1967. Some methods for classification and analysis of multivari-
 1048 ate observations. In *Proceedings of the fifth Berkeley symposium on mathematical*
 1049 *statistics and probability*, Volume 1, pp. 281–297. Oakland, CA, USA.
- 1050 Margules, M. 1903. Über die energie der stürme. *Jahrbuch der Zentralanstalt für*
 1051 *Meteorologie, Wien* 48: Anhang .
- 1052 Marrafon, V.H., M.S. Reboita, R.P. da Rocha, and E.M. de Jesus. 2022. Classificação
 1053 dos tipos de ciclones sobre o oceano atlântico sul em projeções com o regcm4 e
 1054 mcgs. *Revista Brasileira de Climatologia* 30: 1–25 .
- 1055 McErlich, C., A. McDonald, J. Renwick, and A. Schuddeboom. 2023. An assessment
 1056 of extra-tropical cyclone precipitation extremes over the southern hemisphere using
 1057 era5. *Geophysical Research Letters* 50(17): e2023GL104130 .
- 1058 Michaelides, S. 2021. Lorenz atmospheric energy cycle in climatic projections.
 1059 *Climate* 9(12): 180 .

- 1060 Michaelides, S.C. 1987. Limited area energetics of genoa cyclogenesis. *Monthly*
1061 *Weather Review* 115(1): 13–26 .
- 1062 Michaelides, S.C. 1992. A spatial and temporal energetics analysis of a baroclinic
1063 disturbance in the mediterranean. *Monthly weather review* 120(7): 1224–1243 .
- 1064 Michaelides, S.C., N.G. Prezerakos, and H.A. Flocas. 1999. Quasi-lagrangian ener-
1065 getics of an intense mediterranean cyclone. *Quarterly Journal of the Royal*
1066 *Meteorological Society* 125(553): 139–168 .
- 1067 Muench, H.S. 1965. On the dynamics of the wintertime stratosphere circulation.
1068 *Journal of Atmospheric Sciences* 22(4): 349–360 .
- 1069 Novak, L. and R. Tailleux. 2018. On the local view of atmospheric available potential
1070 energy. *Journal of the Atmospheric Sciences* 75(6): 1891–1907 .
- 1071 Okajima, S., H. Nakamura, and Y. Kaspi. 2021. Cyclonic and anticyclonic contribu-
1072 tions to atmospheric energetics. *Scientific reports* 11(1): 13202 .
- 1073 Oort, A.H. 2018. On estimates of the atmospheric energy cycle, *Renewable Energy*,
1074 Vol1.214–Vol1.235. Routledge.
- 1075 Pan, Y., L. Li, X. Jiang, G. Li, W. Zhang, X. Wang, and A.P. Ingersoll. 2017. Earth’s
1076 changing global atmospheric energy cycle in response to climate change. *Nature*
1077 *communications* 8(1): 14367 .
- 1078 Pezza, A.B., L.A. Garde, J.A.P. Veiga, and I. Simmonds. 2014. Large scale features
1079 and energetics of the hybrid subtropical low ‘duck’over the tasman sea. *Climate*
1080 *dynamics* 42: 453–466 .
- 1081 Pezza, A.B., J.A.P. Veiga, I. Simmonds, K. Keay, and M.d.S. Mesquita. 2010. Envi-
1082 ronmental energetics of an exceptional high-latitude storm. *Atmospheric Science*
1083 *Letters* 11(1): 39–45 .
- 1084 Rantanen, M., J. Räisänen, V.A. Sinclair, and H. Järvinen. 2019. Sensitivity
1085 of idealised baroclinic waves to mean atmospheric temperature and meridional
1086 temperature gradient changes. *Climate Dynamics* 52: 2703–2719 .
- 1087 Read, P., D. Kennedy, N. Lewis, H. Scolan, F. Tabataba-Vakili, Y. Wang, S. Wright,
1088 and R. Young. 2020. Baroclinic and barotropic instabilities in planetary atmo-
1089 spheres: energetics, equilibration and adjustment. *Nonlinear Processes in Geo-*
1090 *physics* 27(2): 147–173 .
- 1091 Reboita, M.S., R.P. Da Rocha, T. Ambrizzi, and S. Sugahara. 2010. South atlantic
1092 ocean cyclogenesis climatology simulated by regional climate model (regcm3).
1093 *Climate Dynamics* 35: 1331–1347 .

- 1094 Reboita, M.S., R.P. da Rocha, M.R. de Souza, and M. Llopart. 2018. Extratropi-
 1095 cal cyclones over the southwestern south atlantic ocean: Hadgem2-es and regcm4
 1096 projections. *International Journal of Climatology* 38(6): 2866–2879 .
- 1097 Reboita, M.S., M.A. Gan, R. Da Rocha, T. Ambrizzi, et al. 2010. Precipitation regimes
 1098 in south america: a bibliography review. *Revista Brasileira de Meteorologia* 25(2):
 1099 185–204 .
- 1100 Rudeva, I. and S.K. Gulev. 2007. Climatology of cyclone size characteristics and their
 1101 changes during the cyclone life cycle. *Monthly Weather Review* 135(7): 2568–2587 .
- 1102 Savita, A., J. Kjellsson, R.P. Kedzierski, M. Latif, T. Rahm, S. Wahl, and W. Park.
 1103 2023. Assessment of climate biases in openifs version 43r3 across model horizontal
 1104 resolutions and time steps. *Geoscientific Model Development Discussions* 2023:
 1105 1–25 .
- 1106 Sinclair, M.R. 1994. An objective cyclone climatology for the southern hemi-
 1107 sphere. *Monthly Weather Review* 122(10): 2239–2256. [https://doi.org/10.1175/
 1108 1520-0493\(1994\)122<2239:AOCCT>2.0.CO;2](https://doi.org/10.1175/1520-0493(1994)122<2239:AOCCT>2.0.CO;2) .
- 1109 Sinclair, M.R. 1995. A climatology of cyclogenesis for the southern hemisphere.
 1110 *Monthly Weather Review* 123(6): 1601–1619 .
- 1111 Smith, P.J. 1980. The energetics of extratropical cyclones. *Reviews of Geo-*
 1112 *physics* 18(2): 378–386 .
- 1113 Swart, N.C., J.N. Cole, V.V. Kharin, M. Lazare, J.F. Scinocca, N.P. Gillett, J. Anstey,
 1114 V. Arora, J.R. Christian, S. Hanna, et al. 2019. The canadian earth system model
 1115 version 5 (canesm5. 0.3). *Geoscientific Model Development* 12(11): 4823–4873 .
- 1116 Tecchio, R., D.C. de Souza, M.B.L. da Silva, M.C. de Oliveria Costa, R. de Camargo,
 1117 and J. Harari. 2024. Mean sea level, tidal components and surges in guanabara bay
 1118 (rio de janeiro) from 1990 to 2021. *International Journal of Climatology* .
- 1119 Trigo, I.F. 2006. Climatology and interannual variability of storm-tracks in the euro-
 1120 atlantic sector: a comparison between era-40 and ncep/ncar reanalyses. *Climate*
 1121 *Dynamics* 26(2): 127–143 .
- 1122 Veiga, J.A.P. and T. Ambrizzi. 2013. A global and hemispherical analysis of the
 1123 lorenz energetics based on the representative concentration pathways used in cmip5.
 1124 *Advances in Meteorology* 2013(1): 485047 .
- 1125 Veiga, J.A.P., A.B. Pezza, I. Simmonds, and P.L. Silva Dias. 2008. An analysis of the
 1126 environmental energetics associated with the transition of the first south atlantic
 1127 hurricane. *Geophysical Research Letters* 35(15) .

- 1128 Vincent, D. and L. Chang. 1973. Some further considerations concerning energy
1129 budgets of moving systems. *Tellus* 25(3): 224–232 .
- 1130 Wahab, M.A., H.A. Basset, and A. Lasheen. 2002. On the mechanism of winter cyclo-
1131 genesis in relation to vertical axis tilt. *Meteorology and Atmospheric Physics* 81(1):
1132 103–127 .
- 1133 Wiin-Nielsen, A. 1968. On the intensity of the general circulation of the atmosphere.
1134 *Reviews of Geophysics* 6(4): 559–579 .
- 1135 Young, R. 2014. The lorenz energy cycle in simulated rotating annulus flows. *Physics*
1136 *of Fluids* 26(5) .
- 1137 Zheng, Z. 2021. zzheng93/pyeof: First release (v0.0.0).

1138 Supplementary information

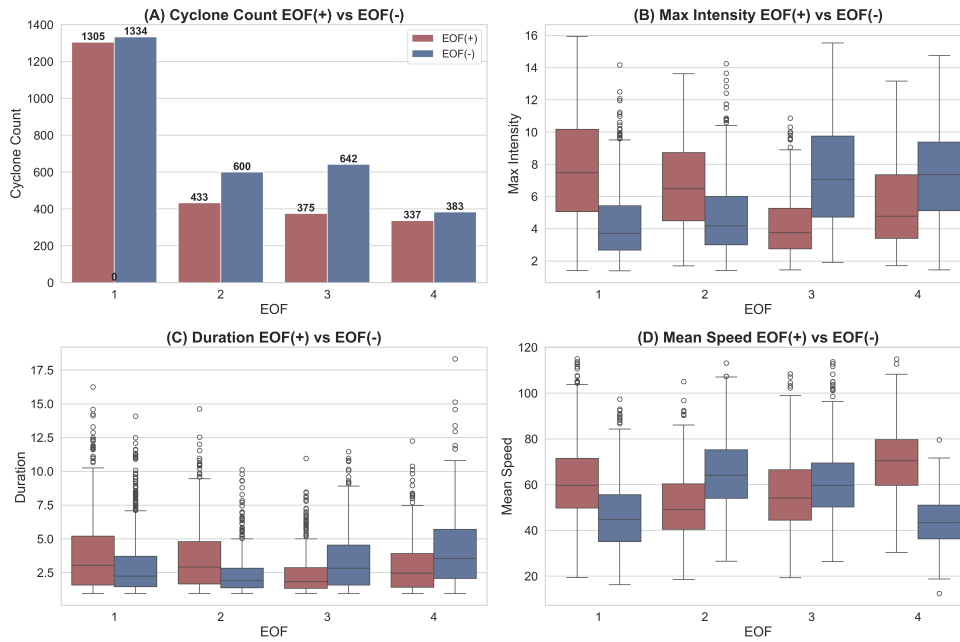


Fig. S1 Statistics for the cyclones classified as EOF(+) (red) and EOF(-) (blue). (A) Cyclone counts; (B) maximum intensity, expressed by the *minimum* central relative vorticity at 850 hPa; (C) total life-cycle duration (days); and (D) mean translational speed (km h⁻¹).

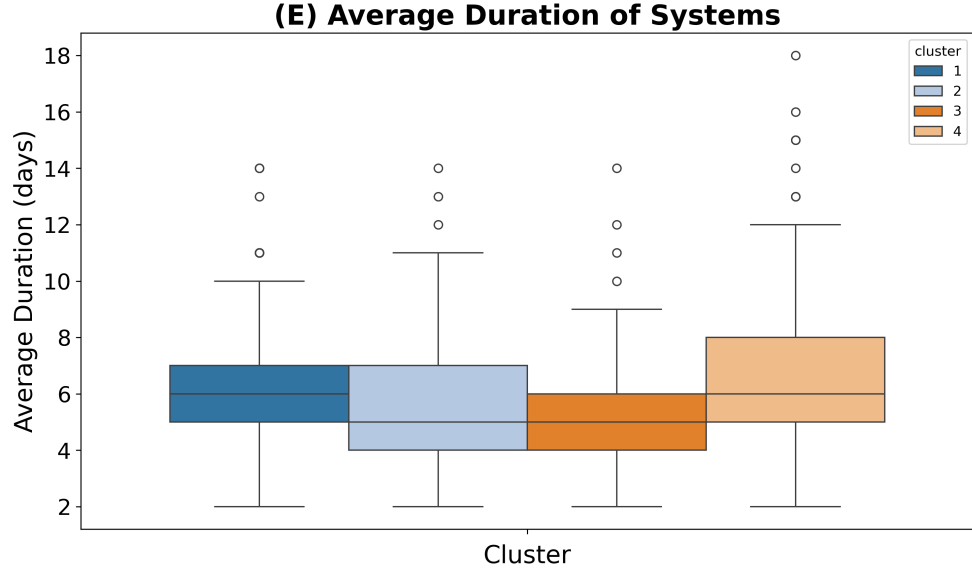


Fig. S2 Boxplot of the total life cycle duration (in days) for the four clusters (1–4) identified among the most intense cyclones in the dataset.

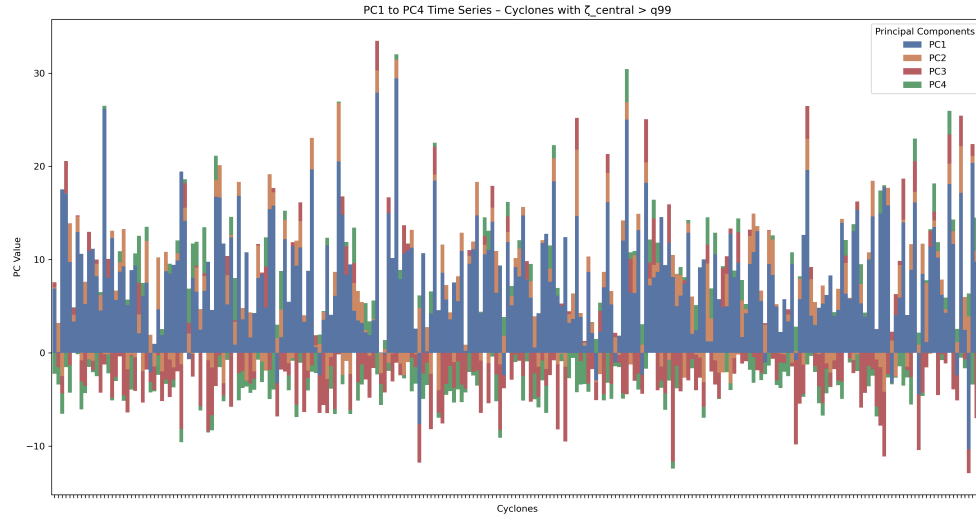


Fig. S3 Stacked time series of the first four principal components (PC1–PC4) for each intense cyclone ($\zeta_{850, \text{max}} > q_{99}$). Positive values are plotted upward and negative values downward, so the coloured bars represent the signed contribution of each EOF mode to the energetics of every system. The x -axis lists the individual cyclones (sorted arbitrarily), while the y -axis gives the PC amplitude (dimensionless).

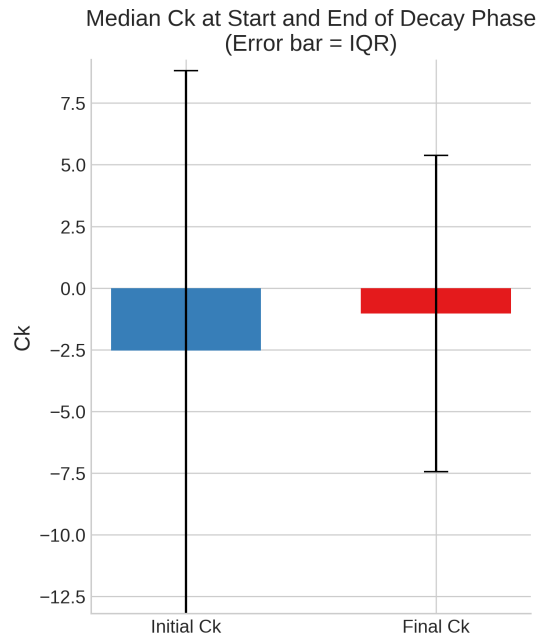


Fig. S4 Median barotropic-conversion term (C_k) at the start (blue) and end (red) of the decay phase, with the error bars representing the inter-quartile range.